frontiers in Earth Science

TYPE Original Research
PUBLISHED 24 March 2026
DOI 10.3389/feart.2026.1778360

Characterizing the subsurface structure and active faults of the Fucino Basin (Central Apennines) through integrated high-resolution seismic reflection and nodal ambient noise surveys

Luigi Improta[1], Stefano Maraio[2], Giuseppe Di Giulio[2], Maurizio Vassallo[2], Marco Massa[3], Sara Lovati[3], Matteo Lupi[4], Fabio Villani[5], Salomon Hailemikael[2], Daniela Famiani[2], Alessia Mercuri[2], Paolo Marco De Martini[2]*, Vincenzo Sapia[5], Antonino D'Alessandro[1], Pier Paolo Gennaro Bruno[5,6], Carlo Alberto Brunori[2], Riccardo Civico[2], Alessandra Sciarra[2], Pamela Roselli[2], Anna Figlioli[3], Simona Bongiovanni[7], Stefania Pucillo[8], Gaetano Riccio[8], Rocco Cogliano[8], Giulio Brunelli[3], Salvatore Scudero[1], Stefano Speciale[1], Livio Ruggiero[9], Paola Baccheschi[1], Giovanna Cultrera[2], Stefano Pucci[2], Luisa Valoroso[1], Pasquale De Gori[1], Andrea Rindinella[10], Daniele Silvestri[10], Irene Molinari[11] and Giuliano Milana[2]

[1]Istituto Nazionale di Geofisica e Vulcanologia, Osservatorio Nazionale Terremoti, Rome, Italy, [2]Istituto Nazionale di Geofisica e Vulcanologia, Sismologia e Tettonofisica, Rome, Italy, [3]Istituto Nazionale di Geofisica e Vulcanologia, Sezione di Milano, Milan, Italy, [4]Department of Earth Sciences, University of Geneva, Geneva, Switzerland, [5]Istituto Nazionale di Geofisica e Vulcanologia, Geomagnetismo, Aeronomia, e Geofisica Ambientale, Rome, Italy, [6]Dipartimento di Scienze della Terra, Ambiente e Risorse, Università di Napoli, Naples, Italy, [7]Dipartimento di Scienze della Terra e del Mare, Università di Palermo, Palermo, Italy, [8]Istituto Nazionale di Geofisica e Vulcanologia, Sezione Irpinia, Grottaminarda, Italy, [9]Consiglio Nazionale delle Ricerche (CNR), Ufficio Infrastrutture di Ricerche – DG, Rome, Italy, [10]Centro di Geotecnologie, Università di Siena, San Giovanni Valdarno, Italy, [11]Istituto Nazionale di Geofisica e Vulcanologia, Sezione di Bologna, Bologna, Italy

EDITED BY
Paolo Capuano,
University of Salerno, Italy

REVIEWED BY
Rita De Nardis,
University of Studies G. d'Annunzio Chieti and Pescara, Italy
Riccardo Caputo,
University of Ferrara, Italy
Raffaella De Matteis,
University of Sannio, Italy

*CORRESPONDENCE
Paolo Marco De Martini,
paolomarco.demartini@ingv.it

RECEIVED 30 December 2025
REVISED 20 February 2026
ACCEPTED 23 February 2026
PUBLISHED 24 March 2026

CITATION
Improta L, Maraio S, Di Giulio G, Vassallo M, Massa M, Lovati S, Lupi M, Villani F, Hailemikael S, Famiani D, Mercuri A, De Martini PM, Sapia V, D'Alessandro A, Gennaro Bruno PP, Brunori CA, Civico R, Sciarra A, Roselli P, Figlioli A, Bongiovanni S, Pucillo S, Riccio G, Cogliano R, Brunelli G, Scudero S, Speciale S, Ruggiero L, Baccheschi P, Cultrera G, Pucci S, Valoroso L, De Gori P, Rindinella A, Silvestri D, Molinari I and Milana G (2026) Characterizing the subsurface structure and active faults of the Fucino Basin (Central Apennines) through integrated high-resolution seismic reflection and nodal ambient noise surveys.
Front. Earth Sci. 14:1778360.
doi: 10.3389/feart.2026.1778360

The Fucino Basin, the largest tectonic basin within the Central Apennines orogen, is bounded by normal faults that have controlled the deposition of over 1 km of Pliocene-Quaternary continental deposits above a Messinian substratum. Conflicting interpretations from legacy seismic profiles have hindered a full understanding of the basin's stratigraphy, age, evolution, and fault systems, creating uncertainties for tectonic reconstructions, seismic response analysis and hazard assessment. To resolve these uncertainties, we acquired new high-resolution datasets through three complementary active–passive seismic surveys. These include seismic reflection profiles covering ~10 km, a nodal ambient noise campaign deploying 258 short-period nodes over 16 km^2, preceded by two pilot array tests, and finally a basin-wide ambient noise survey comprising 1-hour recordings at 42 sites. Our analysis focused on the San Benedetto and Trasacco Faults—responsible for the 1915, M7.1, Marsica earthquake—and the main depocenter (the Bacinetto) associated with the San Benedetto Fault. This paper presents experimental setup, recorded data, and initial findings that provide new insights into basin stratigraphy, fault geometry, and spatial distribution of the fundamental resonance frequency (f_0). The seismic reflection data show excellent imaging quality, resolution, and penetration exceeding 1 km. The Bacinetto hosts up to 850–900 m of continuous lacustrine succession and lower fluvio-lacustrine deposits that record sustained syn-sedimentary slip along the San Benedetto Fault from the Late Pliocene to Recent times. No evidence is found for significant synthetic or antithetic faulting beneath the depocenter, contradicting earlier structural models. The intra-basin Trasacco Fault forms a clear basement step and localized sediment thickening that tapers northwestward f_0 varies from 1 to 2 Hz near the basin margins to ~0.2 Hz in the Bacinetto, reflecting progressive sediment thickening, whereas it varies abruptly across fault zones. f_0 estimates from nodal and station data show good consistency.

KEYWORDS

ambient noise data, basin seismic response, extensional basin, high-resolution seismic reflection profiles, nodal arrays, seismic stratigraphy, seismogenic faults

1 Introduction

The Fucino Basin (FB), located within the Central Apennines fold-and- thrust belt, is one of the largest tectonic depressions in the Mediterranean region and hosts a continental infill exceeding 1000 m in thickness. Since the Late Pliocene, basin formation and evolution have been controlled by a complex system of faults with prevailing extensional kinematics. The main fault sets strike SW-NE and NW-SE, and bound the northern and eastern basin borders, respectively (Figures 1A,B) (Cavinato et al., 2002). Over the past three decades, the FB has been the focus of numerous scientific projects driven by two main factors: 1) the presence of a thick lacustrine succession that represents a long and continuous sedimentary record extending back to the Middle Pleistocene at least (Giaccio et al., 2019), and 2) the occurrence of large-magnitude earthquakes (M6-7), including the 1915, M7.1, Marsica event, which caused over 30,000 casualties (Galadini and Galli, 1999 and references therein).

Geological, geophysical, and seismological investigations provided insights into the basin structure and evolution, the geometry and seismogenic potential of its active faults, and the local seismic response (Caielli et al., 2023 and references therein; Cara et al., 2011). Notably, scientific drilling projects enabled the definition of high-resolution tephrostratigraphies and chronologies for the lacustrine record spanning the last 430 ka, providing key constraints for palaeoenvironmental and palaeoclimatic reconstructions of the central Mediterranean region (Giaccio et al., 2024).

The FB sub-surface has been extensively investigated, primarily through the re-interpretation of legacy seismic profiles acquired for hydrocarbon exploration (Figure 1A) (Cavinato et al., 2002; Patacca et al., 2008; Patruno and Scisciani, 2021; Caielli et al., 2023). These studies proposed different interpretations of basin stratigraphy, depositional age of the infill, and architecture of the Pliocene-Quaternary normal fault systems (Figure 2). The main reasons for conflicting interpretations are: (i) the variable quantity and quality of the interpreted seismic profiles, (ii) the absence of deep calibration wells and, most significantly, (iii) inadequate data resolution to accurately image shallow targets, such as the continental fill and intra-basin faults. Consequently, the position and depth of the basin depocenters remain controversial, and the faults geometries and activity are not univocally defined (Figure 2 and Supplementary Figure S1). Such uncertainties critically affect reconstructions of the long-term tectonic evolution and seismic hazard assessment.

To improve understanding of the basin's seismogenic faults, stratigraphy and evolution, in 2022 we acquired high-resolution (HR) seismic data by combining passive and active 2D/3D surveys. Our investigation focused on two key targets: the San Benedetto Fault in the eastern margin and the Trasacco Fault in the western sector, both striking NW-SE and dipping to the SW (Figure 1). The former represents the main bounding fault that controlled the basin's evolution since the Early Pleistocene, whereas the latter is the principal intra-basin fault (Cavinato et al., 2002; Patruno and Scisciani, 2021). Notably, both faults ruptured during the Mw 7.1, 1915 Marsica earthquake and have been identified as sources for Holocene and historical M6-7 events, thanks to several paleoseismological studies (Galadini and Galli, 1999).

We carried out three complementary surveys:

a. Reflection Profiling. We acquired four HR reflection profiles for a total length of approximately 10 km (Figure 1A) to obtain the first detailed images of fault-zones and basin stratigraphy down to 500–1000 m-depth. Specific goals were to: (i) constrain the geometry of the San Benedetto and Trasacco faults where they are buried beneath thick, recent sediments, (ii) investigate the internal architecture of the fault zones and the style of deformation in the pre-Pliocene units and shallow sediments, (iii) obtain a high-quality image of the infill stratigraphy within the Bacinetto depocenter, associated with the San Benedetto Fault (Figure 1A).
b. Nodal Ambient Noise Array. A seismic array consisting of 258 three-component, 4.5 Hz and 5.0 Hz nodal seismometers (nodes; Dean et al., 2018) was deployed in the south-western

10.3389/feart.2026.1778360

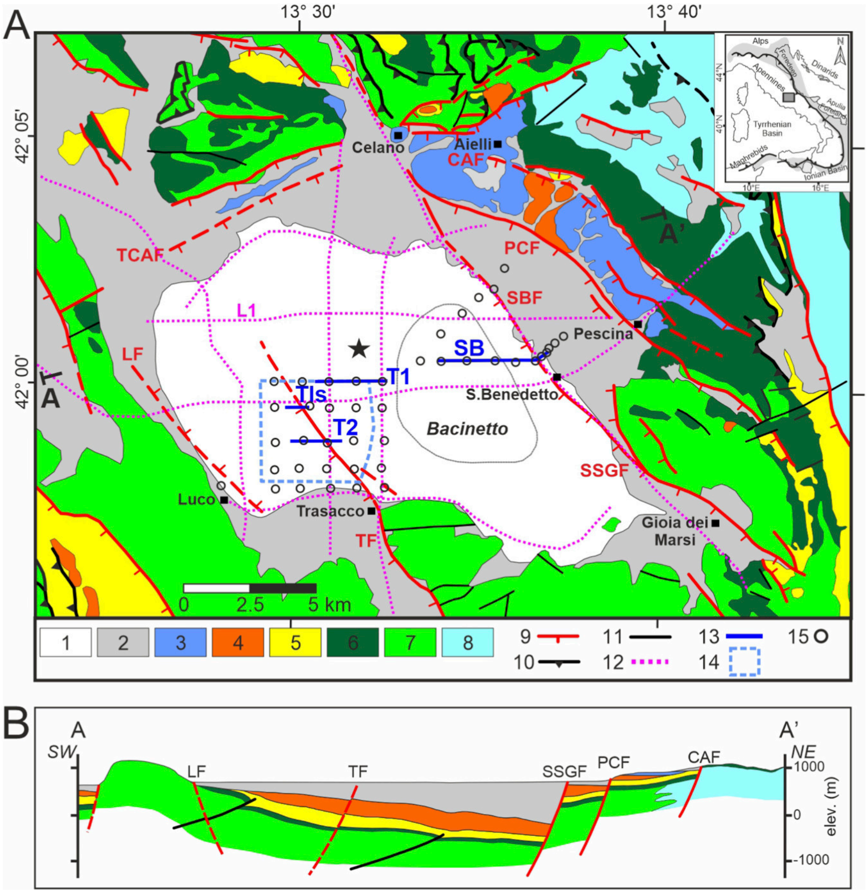

FIGURE 1
(A) Synthetic geological map of the Fucino region (modified after Caielli et al., 2023; Mondati et al., 2021; Faure Walker et al., 2021). 1, Lacustrine deposits (Holocene lake); 2, Lacustrine, fluvio-lacustrine, alluvial and talus deposits (Middle Pleistocene to Recent); 3, Talus, alluvial fan, fluvio-lacustrine deposits (Late Pliocene - Early Pleistocene); 4, brackish deposits of late-orogenic thrust-top basins (Late Messinian); 5, Foredeep flysch deposits (Early Messinian); 6, Miocene carbonate ramp successions (Middle-Late Miocene); 7, Platform carbonates (Mesozoic); 8, Slope-to-basin carbonates (Mesozoic-Paleogene); 9, Pliocene-Quaternary normal faults; 10, Thrust faults; 11, Subsidiary faults; 12, Seismic commercial profiles (the profile labelled L1 is shown in Figure 11); 13, High-resolution seismic profiles labelled SB, T1, T2, and Tls (this study); 14, Nodal array survey area; 15, Noise measurements by stand-alone seismic stations equipped with 5s seismometers. The black star denotes the epicentre of the 1915 Marsica earthquake (Rovida et al., 2021). Main normal fault systems: SSGF, San Benedetto - Serrone - Gioia dei Marsi fault system; SBF, San Benedetto Fault; PCF, Pescina - Celano fault; CAF, Collarmele - Aielli fault; TCAF, Tre Monti - Celano - Aielli fault; TF, Trasacco Fault; LF, Luco dei Marsi Fault. **(B)** Simplified geological section across the Fucino Basin (modified after Caielli et al., 2023; Mondati et al., 2021). The extremes of this geological section are highlighted in the map with labels A-A′.

sector of the basin, spanning the presumed trace of Trasacco Fault (Figure 1A). The array covered an area of 16 km^2 and operated continuously for approximately 3 weeks. Two preparatory smaller arrays of seismic nodes were deployed for several hours to assess the overall characteristics of the ambient noise. The experiment had the main goal to collect ambient noise data to investigate the seismic response in settings of high structural complexity and the shallow S-wave velocity structure across the Trasacco fault zone. The array was crossed by three HR seismic profiles allowing constraints on the subsurface structure (Figure 1A).

c. Large-Scale Ambient Noise Survey. One-hour-long ambient noise recordings were additionally acquired in 42 sites, covering a large part of the FB, using seismic stations equipped with 5s velocimeters (Figure 1A). In the eastern sector, stations were deployed along two W-E transects across the San Benedetto Fault and the Bacinetto depocenter to investigate the seismic response at sharp lateral lithological changes. Numerous stations were co-located with the HR seismic profiles to constrain the interpretation of the noise analysis, and with the nodal array sites to compare results obtained from recordings of varying lengths and instrumentation.

This paper introduces the Fucino Basin passive-active seismic experiment. We first outline the geological and seismotectonic setting of the FB, emphasizing inconsistencies among published subsurface geological models. We then describe the objectives and design of our integrated seismic surveys. Next, we present the acquired seismic data, with a focus on their quality. Finally, we discuss the initial findings of the data analysis, which provide new insights into basin stratigraphy, geometry of the San Benedetto and Trasacco faults, and the basin's fundamental resonance frequency. These findings highlight important methodological considerations for seismic investigation of structurally complex, fault-controlled basins.

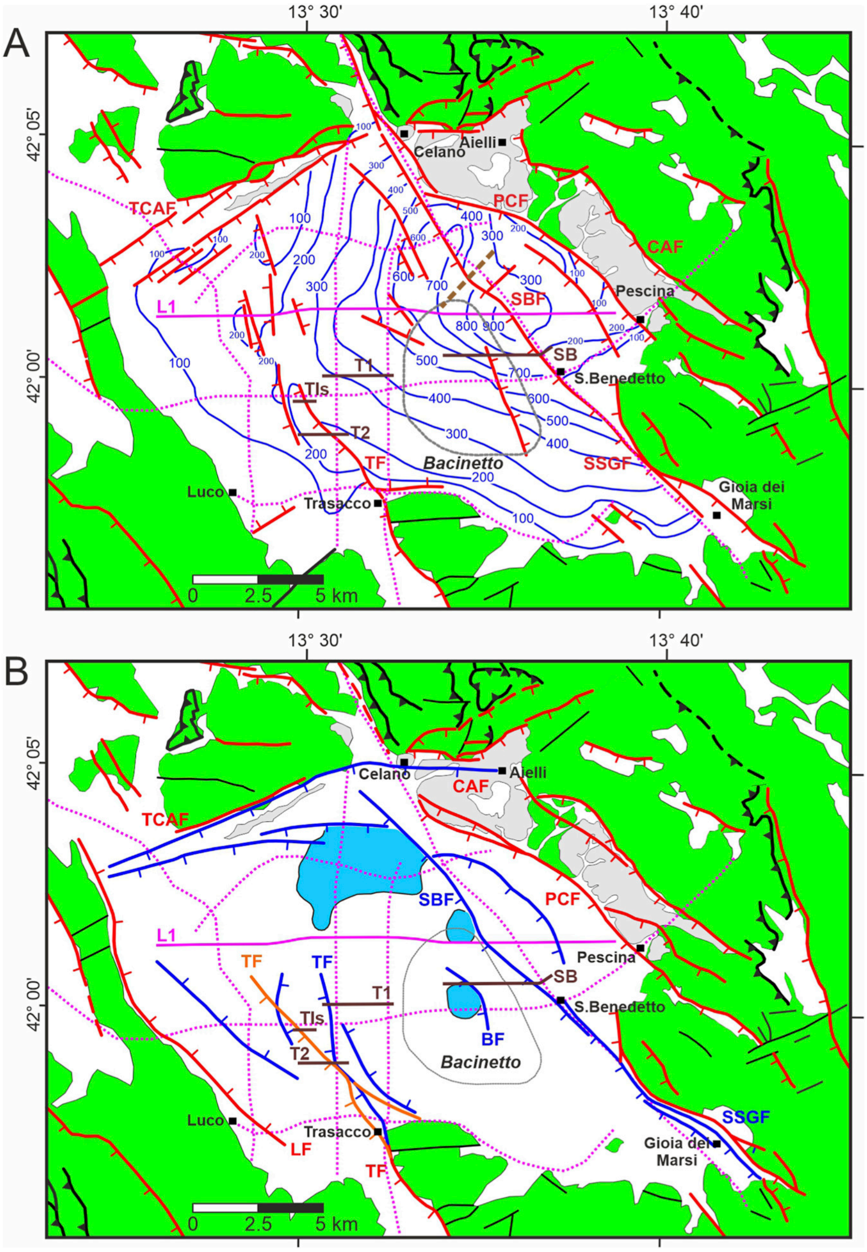

FIGURE 2
Subsurface structure of the Fucino Basin. **(A)** Subsurface model redrawn from Cavinato et al. (2002). Red lines denote Pliocene-Pleistocene normal faults identified in the subsurface by interpreting seismic commercial profiles (dotted magenta lines). Blue lines are the isochron contours (interval 100 ms TWT) of the Upper Pliocene to Recent continental deposits. The pre-Pliocene geological units are shown in green, the Upper Pliocene - Lower Pleistocene continental deposits are shown in gray (modified after Caielli et al., 2023; Mondati et al., 2021; Faure Walker et al., 2021). The magenta continuous line denotes the commercial profile L1 shown in Figure 11. The high-resolution seismic profiles SB, T1, T2 and Tls (this study) are shown with brown lines. The brown dashed line evidences the northern transect of single-station noise measurements. **(B)** Subsurface model redrawn from Patruno and Scisciani (2021). Blue lines denote Plio-Pleistocene faults detected in the subsurface by interpreting seismic commercial profiles (dotted magenta lines), while the faults mapped from outcrops are shown with red lines. The sky-blue regions denote the basin depocenters reported by Patruno and Scisciani (2021) and correspond to basin sectors where the total thickness of the Pliocene-Quaternary continental succession exceeds 1350 ms TWT. Normal fault systems: SSGF, San Benedetto - Serrone - Gioia dei Marsi fault system; SBF, San Benedetto Fault; PCF, Pescina - Celano fault; CAF, Collarmele - Aielli fault; TCAF, Tre Monti - Celano - Aielli fault; TF, Trasacco Fault; LF, Luco dei Marsi Fault; BF, Bacinetto Fault. The Trassaco Fault traced inside the basin by Faure Walker et al.
(2021) is shown with a thick orange line.

2 Background

2.1 Geological setting

The Central Apennines range is a Neogene, NE-verging fold-and- thrust belt developed due to the deformation of the Adria continental margin, linked to the eastward retreat of the Adria-Ionian slab (Malinverno and Ryan, 1986). The study region has experienced NE-SW regional extension since the Late Pliocene (Cosentino et al., 2017), with deformation primarily accommodated by normal fault systems that are typically NW-SE striking, SW-dipping and 20–30 km-long (Faure Walker et al., 2021, and references therein).

Subsurface models based on legacy seismic commercial profiles define the FB as a half-graben type basin (Figure 1B). The basin is filled by Late Pliocene to Recent continental sequences that gently dip NW-ward and NE-ward in the hangingwall of the bounding faults (Patacca et al., 2008) (Figure 1A). The basin substratum consists of Meso-Cenozoic slope-to-basin and platform carbonates, unconformably overlain by syn-orogenic and late-orogenic Messinian siliciclastic deposits (Cavinato et al., 2002; Mondati et al., 2021; Caielli et al., 2023). These folded and thrusted pre-Pliocene units were in turn dissected by Pliocene-Quaternary fault systems with normal to oblique kinematics, which bound the FB with two trends: WSW-ENE to the north and NNW-SSE to the east (Figure 1A) (Galadini and Messina, 1994). This large-scale geometry of the basin is confirmed by gravity data modelling (Mancinelli et al., 2021; Cella et al., 2021).

Surface geological data and commercial reflection profiles indicate that the evolution of the basins has been controlled by two main fault systems: the WSW-ENE trending, SSE-dipping Tre Monti - Celano - Aielli fault system to the north (TCAF in Figure 1A), and the NNW-SSE trending, WSW-dipping San Benedetto - Serrone - Gioia dei Marsi fault system (SSGF) to the east [Caielli et al. (2023) and references therein]. In the literature, the general evolutionary model of the FB involves the time-delayed activation of these two systems, resulting in a polyphase evolution with important changes in the depositional setting (Galadini and Messina, 1994; Galadini and Galli, 1999; Cavinato et al., 2002; Patacca et al., 2008; Patruno and Scisciani, 2021; Caielli et al., 2023). The TCAF was significantly active during the Late Pliocene-Early Pleistocene with right-lateral transtensional kinematics, leading to the deposition of breccia, alluvial and lacustrine sequences primarily in the northern and northwestern sectors of the basin. Conversely, the SSGF has been characterised by intense Quaternary activity. This fault system has controlled the growth and syn-sedimentary eastward tilting of a wedge of lacustrine, fluvial-deltaic and alluvial deposits, which are several hundreds of meters thick in the central and eastern FB (Figure 1B) [see Lanari et al. (2021) and Caielli et al. (2023) for a review].

Notwithstanding the current consensus relative to the basin evolutionary model, studies based on seismic commercial profiles and surface geological data have yielded different interpretations. These differences pertain to the geometry of the major and secondary fault systems, the position and thickness at the depocenters, the basin stratigraphy, and the depositional age of the sedimentary sequences. Furthermore, the architecture of the active fault systems covered by thick continental sequences is not defined univocally. These discrepancies mainly arise from: (i) variable quality and coverage of legacy seismic profiles, (ii) the lack of deep calibration wells, and (iii) resolution of commercial data insufficient to image shallow deposits and intra-basin faults.

In the following section, we emphasize the main differences among the published subsurface models.

In earlier subsurface models (Cavinato et al., 2002; Patacca et al., 2008), the main depocenter is in the central-eastern FB (i.e., underneath the Bacinetto; see Figure 2A), and its position and evolution were controlled by the northern segment of the SSGF, the San Benedetto Fault. The depocenter is filled with Late Pliocene to Recent continental deposits reaching a thickness of 900 ms TWT (converted to approximately 850 m by Cavinato et al., 2002) in correspondence of the maximum fault throw (about 600 ms TWT) (see Figure 2A). Conversely, the thickness of continental deposits in the hangingwall of the TCAF in the northern FB is significantly smaller (<200–250 ms TWT).

In a recent study, Caielli et al. (2023) partially revised this model after the re-interpretation of a legacy industry profile and a refraction tomography of the CROP11 deep-crustal seismic survey. These authors emphasised the importance of a late-orogenic sequence, consisting of Upper Messinian brackish and siliciclastic deposits, which they ascribed to a thrust-top basin emplaced upon the Meso-Cenozoic carbonate and flysch units (Cipollari et al., 1999; Mondati et al., 2021). Unlike earlier interpretations, the Caielli et al. (2023) subsurface model defines this late-orogenic sequence as a continuous body up to 500 m-thick, that forms the pre-Pliocene substratum across a wide sector of the basin (Figure 1B and Supplementary Figure S1). In the area of the main depocenter, the Upper Pliocene - Pleistocene continental deposits, which unconformably cover the Upper Messinian sequence, reach a thickness of 1050 m TWT. Here, the San Benedetto Fault's maximum throw is estimated to be approximately 550 ms TWT (Supplementary Figure S1).

Patruno and Scisciani (2021) presented a different interpretation of the basin stratigraphy and fault architecture, based on a partial re-processing of the legacy seismic lines. The authors emphasise the importance of WSW-ENE trending, south-dipping normal faults along the northern basin margin, such as the TCAF. They propose that the activity of these northern faults generated the main fault-controlled depocenter, which they locate in the northeastern sector of the FB (Figure 2B). This depocenter reaches a depth of 1450 ms TWT (estimated depth of approximately 1750 m according to the authors) and is mainly filled with Upper Pliocene - Lower Pleistocene continental deposits. Patruno and Scisciani (2021) also propose a different architecture of the SSGF. Their model includes an important splay fault, synthetic to the San Benedetto Fault in the eastern FB, namely, the Bacinetto Fault (labelled BF in Figure 2B). Due to the concurrent activity of these two faults, an easterly polarity affected the basin evolution since the Early Pleistocene, leading to formation of thick syn-tectonic wedges of continental deposits in the eastern sector of the basin. The two faults are associated with distinct depocenters (Figure 2B) that are emplaced on the pre-Pliocene substratum and mainly filled with Lower Pleistocene - Holocene lacustrine deposits. The San Benedetto Fault depocenter reaches a depth of approximately 1400 ms TWT, while the Bacinetto Fault depocenter is 1450 ms TWT deep (corresponding to an estimated depth of approximately 1600 m). Both faults have accumulated a maximum throw in the order of 550–650 m.

The differences between the subsurface models of Patruno and Scisciani (2021) and Caielli et al. (2023) are evident in their interpretations of the best-quality legacy seismic profile L1, which crosses the San Benedetto Fault depocenter (Supplementary Figure S1). Specifically, the thickness of Upper Pliocene to Recent lacustrine and alluvial deposits in the fault hangingwall is reported as 1050 ms TWT by Caielli et al. (2023), compared to 1400 ms TWT by Patruno and Scisciani (2021). This discrepancy primarily stems from the contrasting interpretation of deep seismic units ascribed to Messinian thrust-top and flysch deposits by Caielli et al. (2023), and to Upper Pliocene - Lower Pleistocene continental deposits by Patruno and Scisciani (2021).

Different interpretations have also been proposed for the architecture of the easternmost faults (i.e., Pescina-Celano Fault) and the Trasacco Fault (Figures 2A,B). The Trasacco Fault is exposed southwest of the FB (Figure 1), where it produces a clear bedrock scarp along the western slope of a carbonate ridge (e.g., Papanikolaou et al., 2005). To the northwest, where the fault cuts across alluvial fans and lacustrine deposits in the Fucino plain, its subsurface geometry is not defined univocally. According to Patruno and Scisciani (2021), the intra-basin section of the Trasacco Fault delimits a complex NW-SE trending horst-like salient (Figure 2B). Conversely, in Cavinato et al. (2002), the Trasacco Fault is associated with a synthetic splay that produces a step in the substratum with a maximum fault throw of approximately 100 m TWT (Figure 2A). In addition, the fault's northern tip and its total length remain uncertain.

2.2 Seismotectonic setting

The seismogenic nature of the normal faults in the Fucino area is documented by the 1915 Marsica earthquake (Oddone, 1915; Serva et al., 1988). This event generated coseismic surface ruptures along the NW-SE striking faults on the eastern basin side and along the Trasacco Fault. Several continuous fresh bedrock scarps, up to 1 m high, were observed along the SSGF, and interpreted as the surface expression of coseismic rupture propagating from seismogenic depth along the causative fault. Surface faulting also affected recent lacustrine deposits along the San Benedetto Fault.

Paleoseismic studies of the SSGF and the Pescina-Celano fault allowed to identify at least eleven surface-faulting paleo-earthquakes comparable to the 1915 event, and to estimate Late Pleistocene-Holocene vertical slip rates in the range of 0.35–0.50 mm/yr (Michetti et al., 1996; Galadini et al., 1997; Galadini and Galli, 1999; Galli et al., 2008). Along the intra-basin section of the Trasacco Fault, seven 1915-like paleo-earthquakes were recognized over the past 12 kyr, yielding a short-term vertical slip rate of 0.3–0.4 mm/yr (Galadini et al., 1997). The vertical slip rate decreases toward the northwest, from 0.38 mm/yr (inferred 3 km south of Trasacco village; Papanikolou et al., 2005) to 0.08 mm/yr (derived 7 km north of Trasacco), consistent with slip tapering toward the fault's northern edge (Galadini et al., 1997).

Following the 1915 Marsica earthquake, the Fucino area has been characterized by a low rate of seismicity (Rovida et al., 2021). Only 104 local events of low-to-moderate magnitude (M_L = 2.0–4.1) were recorded over the last four decades by the Italian National Seismic Network run by Istituto Nazionale di Geofisica e Vulcanologia (INGV). The background seismicity recorded between April 2003–September 2004 by a regional temporary network confirmed that the Fucino fault systems are characterized by a low level of seismicity (Bagh et al., 2007).

Cara et al. (2011) investigated the basin seismic response through the analysis of small to moderate local and regional earthquakes. Data recorded at 16 sparse sites revealed strong ground motion amplifications relative to hard-rock reference stations. Remarkable amplifications characterize the sites located west of the San Benedetto Fault and within the Bacinetto. Here, low-frequency amplification peaks (<1 Hz) define the basin's fundamental resonance frequency. At the basin edges, ground motion amplifications shift towards higher frequencies (>1 Hz). The resonance frequencies (f_0) inferred from horizontal-to-vertical spectral ratios of ambient noise (HVNSR; Nakamura, 1989; Molnar et al., 2022) showed close agreement with those estimated from earthquake data. Single-station ambient noise surveys conducted in the northwestern (Di Naccio et al., 2020) and southwestern basin's margins (Famiani et al., 2022) confirm the gradual decrease in the f_0 value moving from the basin margins toward the plain. The Famiani et al. (2022) survey partly overlaps with our nodal array experiment. Their 88 measurement sites showed f0 values decreasing from 0.9 Hz to 0.4–0.5 Hz in the northeastern direction, correlating with the general thickening of the basin infill, while f_0 values of 1.0–2.5 Hz characterize the basin edge. Local variations in f_0 were also observed across the Trasacco Fault.

3 Seismic data

3.1 High-resolution seismic profiling

We acquired four HR seismic reflection profiles in key sectors of the basin to improve knowledge of the basin's stratigraphy and of the geometry and activity of the San Benedetto and Trasacco faults, providing better constraints than to legacy commercial surveys. Each seismic profile was designed with specific targets in mind, but local logistic constraints influenced the acquisition geometry. The Fucino plain is characterized by an orthogonal network of mostly unpaved roads, which are oriented E-W and N-S, parallel to the main drainage canals. Accordingly, we utilized an E-W direction for all seismic lines (Figure 1A), which allows better investigation of the E-dipping syn-sedimentary wedges and NNW-SSE striking faults. The four HR profiles are:

a. San Benedetto profile (SB) is 4200-m-long and crosses the San Benedetto Fault and the Bacinetto depocenter (Figure 1A). It aims to: investigate the sedimentary sequence in both the fault footwall and hangingwall, where the lacustrine sequence reaches its maximum thickness, reconstruct the internal architecture of the fault zone, assess changes in faulting and deformation style moving from the brittle limestone substratum to the ductile lacustrine sequence, and detect active fault splays potentially associated with surface faulting hazard.
b. Trasacco profile (T1) is 2700-m-long and crosses the central sector of the basin (Figure 1A). It targets

the basin's infill and substratum, and possible active faults in the footwall of the Trasacco Fault. This profile is tied to the deepest scientific drillings in the plain [wells F4-F5 analysed by Giaccio et al. (2017), Giaccio et al. (2019) and Giaccio et al. (2024)], reaching a depth of 98 m, and aims at correlating high-resolution seismic stratigraphy with well-based tephrostratigraphies and chronologies.

c. Trasacco profile (T2) is 1915-m-long and crosses the Trasacco fault-zone (Figure 1A). Its main objective is to constraint the position, architecture, and total throw of this fault, which remains debated in the literature (Figures 2A,B).
d. Land Streamer profile (Tls) is 900-m-long and crosses the northernmost section of the Trasacco fault-zone. It was designed to test the effectiveness of a land-streamer system developed by INGV for imaging deep continental basins in areas affected by high cultural noise, and to further constrain fault geometry.

All seismic data were collected by using a 6-ton vibratory source (IVI Minivib vibroseis). Except for the land streamer survey, the acquisition system consisted of twelve 24-channels Geode (Geometrics) seismographs connected to 288, 4.5 Hz, vertical geophones. The source and geophone spacing were 10 m and 5 m, respectively. The deployed linear array of geophones allowed a maximum source-receiver offset of 1435 m, and it was shifted using the roll-along technique to acquire the full-length of each profile. The positions of all shots and geophones were accurately measured using high-precision GPS. The seismic profiles were acquired over 10 days (June-July 2022) by a field team composed of 10–12 researchers.

Data were acquired using a multi-fold wide-aperture geometry, which allows the simultaneous collection of: 1) near-vertical reflection data and post-critical wide-angle reflections generated by deep interfaces, and 2) redundant first arrivals corresponding to shallow direct waves, deep penetrating turning waves, and critical refractions. The objective is to derive complementary seismic reflection images and P-wave velocity refraction tomography models (Improta and Bruno, 2007). With this acquisition configuration, we achieved a maximum common-mid-point (CMP) redundancy of 72, which is high for high-resolution profiles spanning kilometres.

Unlike the standard reflection setup described above, the land streamer survey acquisition system consists of a modular system of 24-channels Geode seismographs and 48 mobile iron plates, each mounting a pair of vertical geophones operating in stacking mode. The streamer is connected to the vibroseis truck to acquire data with an end-on roll-along geometry. In this experiment, we used a source and receiver spacing of 5 m and 10 Hz vertical geophones. The streamer was 235 m-long with minimum and maximum source-receiver offset of 35 and 270 m, respectively. With this acquisition layout, we collected near-vertical reflection data with a nominal maximum midpoint coverage of 24-fold. The land-streamer line is 885 m-long and was acquired along a straight paved road. This experiment lasted 1 day and involved four researchers.

Besides the road network, significant logistic challenges for HR seismic profiling were posed by irrigation channels, which interfered with the vibroseis route, and by a stream nearly parallel to the San Benedetto Fault. This stream is responsible for the crooked geometry of the SB line. Furthermore, the seismic profiles were traced to avoid important sources of cultural noise, such as well pumps and farms.

The quality of the recorded data in the eastern and central sectors of the basin ranges from good to excellent (Supplementary Figure S2). Shot gathers for profiles SB and T1 show clear reflection hyperbolas with apices between ~100 and 800–900 m TWT. Reflectivity is very high. Large amplitude reflections from deep interfaces are evident in the intermediate to large offset range, down to 1400 ms TWT. Most shot gathers display clear first arrivals, up to maximum recording distance of 1435 m (Supplementary Figures S2, S3). These first breaks define arrival-time curves with apparent P-wave velocity weakly increasing with distance from ~900 to 1400 m/s. This indicates turning waves propagating within a low-velocity medium with a weak vertical velocity gradient, consistent with a several-hundred-meter-thick lacustrine sequence. Shot-gathers for profile T1 also exhibit clear large-offsets refractions with apparent velocity of 3000–3300 m/s (Supplementary Figure S2), which can be interpreted as head-waves generated at the top of the Messinian units (Caielli et al., 2023). Given the high-quality large-offset refraction data, seismic tomography is expected to image the basin substratum too.

Data acquired in the southwestern sector of the basin along profile T2 are of good quality (Supplementary Figure S3). Compared to profiles SB and T1, reflectivity is lower, likely due to an increased lithological variability, associated with interbedded fine-grained lacustrine and coarser alluvial deposits near the basin margin. Very clear refractions at large offset, marked by a distinct knee in the first-arrival traveltime curves, correspond to head-waves propagating within the high-velocity substratum.

The land streamer also yielded good-quality reflection data (Supplementary Figure S3). Large-amplitude, coherent, and laterally continuous reflected phases are evident at offsets larger than 100 m down to 700–900 ms TWT.

3.2 The nodal array experiments

A main array experiment was carried out in the south-western sector of the basin crossed by the intra-basin portion of the Trasacco Fault (Figures 3, 1A). We deployed 258 nodes over an area of 16 km^2 to collect dense noise data. We selected the Trasacco area based on the following reasons: (i) subsurface geological models (Cavinato et al., 2002; Patruno and Scisciani, 2021) show important heterogeneities caused by the fault activity and by the presence of both coarse and fine continental deposits; (ii) the architecture of the fault-zone is not defined univocally (Figures 2A,B); (iii) the new high-resolution profiles T1, T2 and Tls and three legacy commercial lines (Figure 1A) provide constraints for the interpretation of ambient noise data.

In the surveyed area, the thickness of the Pliocene-Quaternary deposits ranges from about 100 m to the south to 300–400 m to the north (Figure 2A). Along the southern margin of the basin, close to Trasacco village, noise spectral analysis of Famiani et al. (2022) defined low-frequency fundamental resonance frequencies (0.4–1 Hz), while surface-wave dispersion curves suggest S-wave velocities between 200 m/s in the near-surface and 600–800 m/s at 50–250 m depth. Based on this preliminary

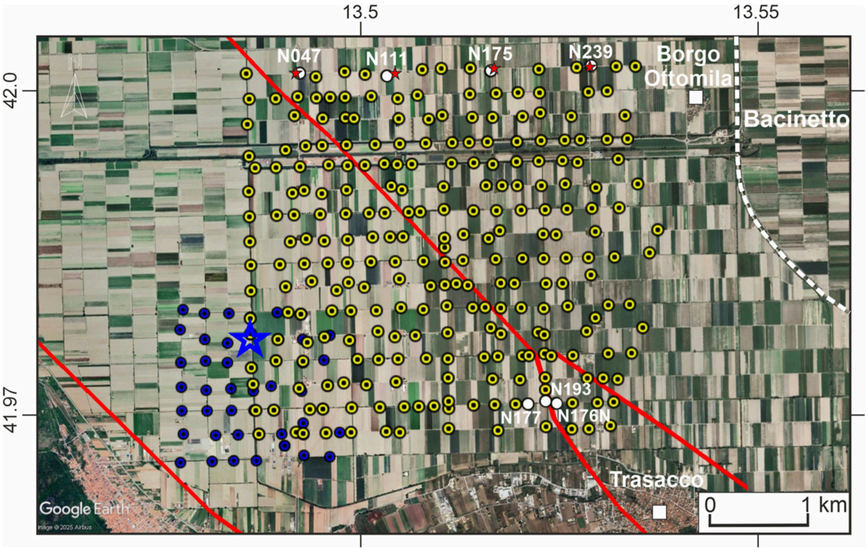

FIGURE 3
Satellite image from Google Earth Pro (https://www.google.com/earth/) illustrates the extent of the nodal array survey in the south-western sector of the Fucino Basin (the array location is reported in Figure 1A). Yellow dots denote the 258 nodes of the three-weeks long experiment. Blue dots denote the 48 nodes of the small-scale 12-hr-long preparatory survey, while the blue star denotes location of the smaller ring-shaped array that operated for several hours. The nodes shown in Figure 14 are labelled and outlined with white dots. The red stars denote co-located stand-alone seismic stations, whose data were used for comparison in Figure 14. The red lines are the trace of Trasacco Fault and Luco Fault (southwest corner) reported by Faure Walker et al. (2021).

information, ambient noise data recorded by a dense nodal array should be suitable to investigate the velocity structure of the whole infill.

To obtain more accurate information on ambient noise that are pivotal to optimize the nodal array survey in terms of acquisition system and node configuration, and to test preliminarily the performance of seismic nodes in the FB, we deployed two preparatory small scale nodal arrays (Figure 3) that are described in the following section.

3.2.1 The preparatory nodal arrays

A bigger preparatory array (blue dots in Figure 3 and Supplementary Figure S4) was composed of 48 nodes deployed on a rectangular grid with a spacing of approximately 250 m for a total size of 1.6 km × 1.6 km. We used GSB data recorders connected to GS_OneLf 4.5 Hz triaxial geophones. This array operated for an entire night. These nodes were deployed the day after in a smaller ring configuration with a maximum aperture of 100 m to record several hours of ambient noise (blue star in Figure 3 and Supplementary Figure S4). For this second experiment, a Reftek-130 digitizer connected to a Lennartz LE3D/5s velocimeter was co-located to the central node of the array. Both preparatory arrays aim to understand the performance of seismic nodes, in terms of positioning retrieved from the internal GPS, data quality (i.e., noise level) and their suitability for the assessment of the surface-wave features and f0 value, which was expected to be well below the 4.5 Hz eigen-frequency of nodes (Famiani et al., 2022).

Each datalogger/geophone was buried into the ground at a depth of 10–20 cm, and its high-precision positioning was determined by a GNSS device using Real-Time Kinematic (RTK) corrections resulting in horizontal accuracy of 1–3 cm. This position was compared to the internal reading of GSB datalogger that was set to acquire one location every 6 min. A mean error on position of 1.2 and 1.4 m was estimated for the larger and smaller array, respectively (Supplementary Figure S4). We believe this is an acceptable result, considering the offset of about 1.0 m between datalogger and cable-connected geophone.

To assess reliability of the f_0 value from noise measurement, we compared the H/V curves obtained with the co-located GS_OneLf and the LE3D/5s velocimeters (eigen frequency of 4.5 and 0.2 Hz, respectively). The analysis was performed on 2 h of ambient noise data recorded at the centre of the circular array. The H/V curves are similar with a sharp peak at 0.7 Hz (Supplementary Figure S5). The main difference is observed on the amplitude of the H/V peak, which is overestimated by 15% by the GS_OneLf geophone compared to the LE3D/5s velocimeter. The spectral ratios were computed on data without instrumental response removal, as evidenced by the Fourier Amplitude Spectra (FAS) (see Supplementary Figure S5). FASs show a good agreement above the eigen-frequency of the node. Conversely, FASs are very different below the eigen-frequency due to the different instrumental response, but this does not affect the H/V curve and the correct estimate of f_0 at about 0.7 Hz. From this test, we concluded that seismic nodes are effective to detect the resonant frequency in the southwestern FB, where it is expected to be below 1 Hz, and that the differences observed in the amplitude of the H/V curve do not hamper the reconstruction of the f_0 spatial pattern. The feasibility of seismic nodes for yielding reliable H/V curves in the FB is confirmed by additional records from co-located stations equipped with LE3D/5s velocimeters (see *Results and Discussions* Section).

3.2.2 The Trasacco large-scale nodal array

3.2.2.1 Survey geometry

The array geometry was designed based on what we learned through the two preparatory nodal surveys. The logistic conditions, including the need to avoid interference with agricultural activities, and the presumed geometry of the Trasacco fault-zone were considered for defining the geometry of the array. The Fucino plain is crossed by country roads and irrigation channels, striking E-W and N-S, with a quite regular spacing of 250 m and 500 m, respectively (Figure 3). To reduce the risk of node loss during a prolonged deployment, particularly due to intensive farming, the nodes were installed at the edges of agricultural fields, roads or channels. This arrangement resulted in a quite regular grid of 250 m × 250 m spacing (Figure 3). A smaller node spacing of 70–120 m was used near the trace of the fault.

Unlike the two preparatory arrays, we combined two types of nodes for this larger scale survey. We used 210 three-component smart seismic sensors developed by SmartSolo (IGU-16HR 3C, with eigen frequency of 5.0 Hz) and 48 GSB recorders connected to GS_OneLf 4.5 Hz geophones. Both nodes are equipped with a 24-bit receiver, integrated lithium battery, and GPS antenna. The geophone sensitivity is 76.7 V/m/s and 89.4 V/m/s for SmartSolo and GSB nodes, respectively. The SmartSolo and GSB nodes were provided by the University of Geneva and by the INGV-ESITO laboratory, respectively. The position of nodes, which were buried approximately 0.1–0.2 m beneath the surface, was determined by using a GNSS RTK antenna.

3.2.2.2 Ambient noise data acquisition and analysis

The nodal instruments were configured to acquire data at a sampling rate of 250 sps, with high gain (equal to 36 dB) and the GPS set to continuous mode. In this configuration, the array worked continuously for 19 days (on average) since 25 June 2022, at which point the batteries were discharged, resulting in the shutdown of the instruments. During this period, data collection continued uninterrupted. However, two nodes were lost and three were damaged by plowing tractors. Data of these damaged nodes were partially recovered.

As with the preparatory surveys described previously, it was essential to ensure data synchronisation to enable subsequent analysis. To this end, we examined temporal variations in the number of satellites visible at each node. The analysis focused on the two types of nodes installed, and the resulting data were used to compute a Probability Density Function and modal trends representative of the number of satellites visible from the nodes (Supplementary Figure S6). Both SmartSolo and GSB nodes exhibited comparable performance in terms of satellite visibility, receiving GPS signals from at least four satellites during the entire acquisition period, with modal values ranging from eight to ten satellites. A notable deviation occurred between 7-9 July 2022, when only the GSB nodes registered an important increase in the modal number of visible satellites (Supplementary Figure S6). The cause of this anomaly remains unclear.

To investigate ambient noise properties, we computed the Power Spectral Density (PSD) of the three-component continuous recordings. The PSD and the related Probability Density Functions (PDFs) were derived from the waveform data and instrument response files using the Probabilistic Power Spectral Densities (PPSDs) class of ObsPy (https://docs.obspy.org/packages/autogen/obspy.signal.spectral_estimation.PPSD.html) that uses the algorithm created by McNamara and Buland (2004). We get PDFs from the distribution of PSD values across spectral intervals. This helps us to understand the probability of a given seismic signal level occurring within a specified frequency band. The PSDs were computed using one-hour signal windows that overlap by 50%.

Figure 4 shows two examples of PPSDs computed for nodal stations N139 and N209, which represent noisy and quiet sites, respectively. The most probable noise levels recorded at both stations are consistently high. At station N209, the most probable values across all components exceed Peterson's (1993) New High Noise Model (NHNM) within the high-frequency range (0.2–1 s). At longer periods (1–10 s), noise levels decrease substantially and fall between the NHNM and the New Low Noise Model (NLNM) envelopes. In contrast, at station N139, the most probable noise levels are significantly higher, by 10–40 dB, and surpass the NHNM throughout the 0.01–10 s period range. We note that node N139 is located near a heavy traffic road. The 10 s upper limit is adopted in this analysis, as the instrumentation used during the survey provides reliable recordings of ambient noise within this interval.

Figure 4 also presents the temporal evolution of the PSDs, averaged over three frequency bands: 7.2–14 Hz, 0.7–1.4 Hz, and 0.3–0.6 Hz. At the noisiest station (N139), pronounced diurnal variations are evident, with nighttime reductions of 20–30 dB across all bands, reaching minimum values around midnight (UTC). At the quieter station (N209), fluctuations in the 7.2–14 Hz range are present but less pronounced (10–30 dB). Variability in the 0.7–1.4 Hz band is more limited (10–20 dB), while it is negligible in the 0.3–0.6 Hz band. These results indicate the presence of significant anthropogenic contributions depending on the node location.

To obtain a comprehensive characterization across the array, the 90th percentile noise level was calculated for each component using the full dataset at each node. The 90th percentile was selected due to the absence of prior knowledge regarding the noise distribution across sites and frequencies, as it provides a robust estimator less affected by outliers or extreme values than lower percentile. Figure 5 shows the resulting curves. At high frequencies (periods < 0.5 s), inter-station differences of up to 40 dB are observed. At lower frequencies (periods > 1 s), the variation increases, reaching up to 70 dB. However, this behaviour is restricted to a limited subset of stations, where the 90th percentile exhibits a linear increase with period. This station-specific behaviour is corroborated by the probability density functions (PDFs) computed for each component (Figure 5). At periods shorter than 0.1 s, the 90th percentiles display greater dispersion compared with the 0.1–10 s range, where a well-defined maximum is consistently observed across all components. Between 0.2 s and 0.5 s, this maximum exceeds Peterson's (1993) NHNM by up to 30 dB.

To investigate the origin of the linear trend observed in some 90th percentile curves, a spatial distribution of the 90th percentile levels was constructed for periods of 1.6 s and 0.6 s (Figure 6). At 1.6 s, elevated noise levels characterize the northern portion of the array. Here, noisy sites define a W-E oriented belt that coincides with a heavy traffic road. At 0.6 s, this spatial pattern is subtle. Noise levels become more homogeneous across the array, apart

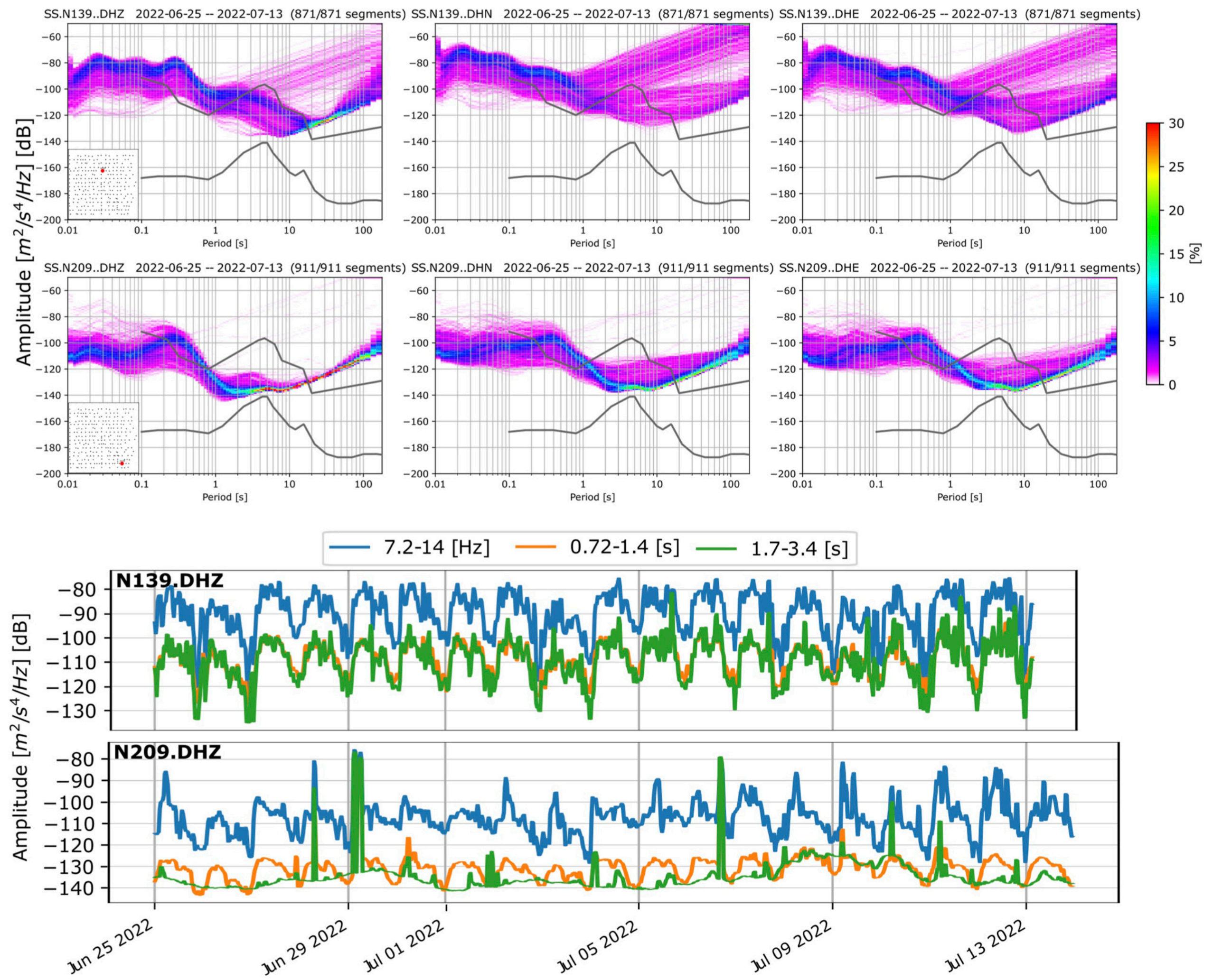

FIGURE 4
Probabilistic power spectral densities (PPSDs) for seismic nodes N139 (top panels) and N209 (central panels), shown for all three components. The positions of the respective nodes within the array are indicated in the insets at the bottom left of the panel related to the vertical components. The PPSDs were computed using the complete dataset acquired during the survey. The two thick lines represent the New High Noise Model and the New Low Noise Model (Peterson, 1993). The two bottom subpanels display the temporal variability of the PSDs recorded by the vertical components of the selected sites across three different frequency bands: 7–14 Hz, 0.7–1.4 Hz (i.e., 0.72–1.4 s in figure) and 0.3–0.6 Hz (i.e., 1.7–3.4 s in figure).

from locally elevated values in the northeastern sector (vertical component), associated with an urbanized area (Borgo Ottomila village highlighted in Figure 3). Conversely, a cluster of stations in the SE records systematically lower noise levels.

3.2.2.3 Earthquake data

No seismic event occurred in close proximity to the nodal array during the experiment. The closest earthquakes recorded by the nodes are eight events with M_L ranging from 0.8 to 2.1, which were located by the Italian National Seismic Network (Margheriti et al., 2021) at epicentral distances of 13–50 km (Ciaccio et al., 2023). Earthquake recordings exhibit low signal-to-noise ratio, mainly due to the high noise levels above 1 Hz (Figure 5). The most energetic seismic phases are observable across the array when the data are low-pass filtered below 1 Hz (Supplementary Figure S7).

Several teleseismic earthquakes were recorded during the experiment. In these cases, the signal-to-noise ratio was significantly higher, as the dominant frequencies of teleseismic signals are well below 1 Hz. An illustrative example is shown in Figure 7, which compares nodal recordings of the 1st July 2022, Mw 6.2, earthquake in Iran, with those of the INGV station PTQR located 7 km northeast of the array and equipped with a broadband velocimeter. Data from the nodal stations and PTQR, corrected for their respective instrument responses and band-pass filtered between 0.05 Hz and 1 Hz (frequencies well below the natural frequency of the nodal geophones), are very similar in both waveform and amplitude. The strong similarity between the seismograms is evident for both the initial arrivals (Figure 7b) and the later surface-wave arrivals (Figure 7d). P-wave first-arrival traveltimes picked at nodes agree with a wavefront propagating across the array from SE to NW (Figure 7c) and picks consistency confirms data synchronisation.

10.3389/feart.2026.1778360

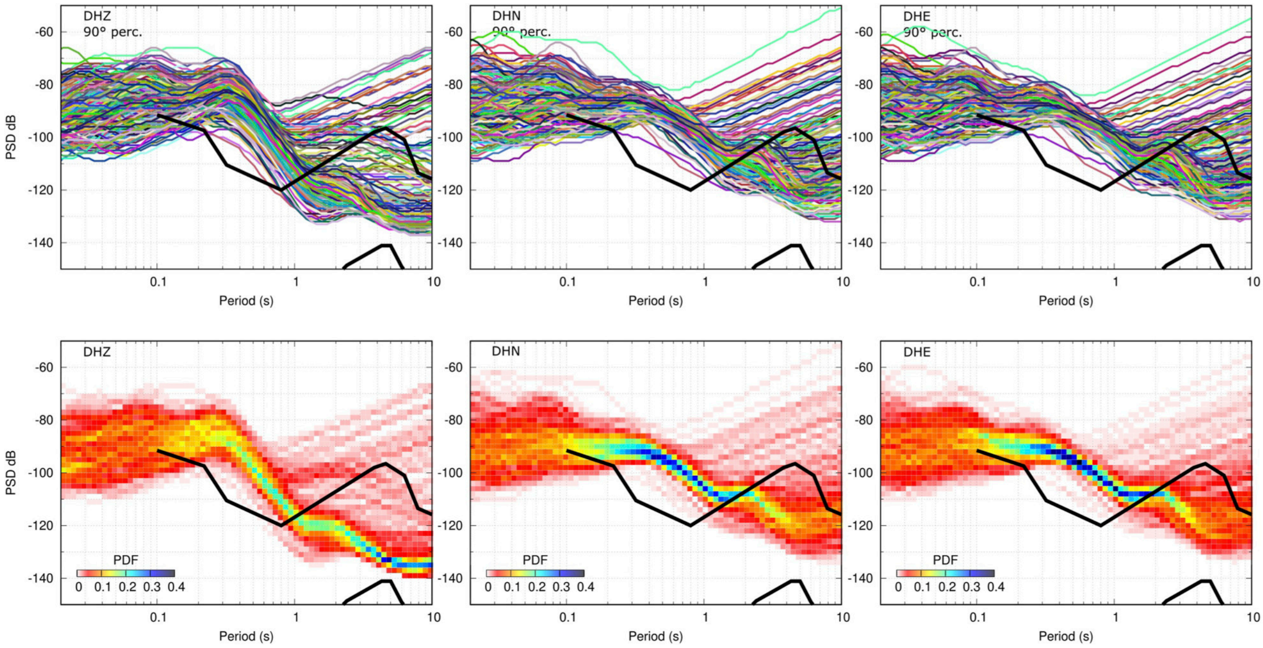

FIGURE 5
Curves of the 90th percentile levels (top subpanels) computed for the 256 recovered nodes for the three components. The bottom subpanels display the probability density functions (PDFs) of the 90th percentile values, derived from all computed curves for each component. The two thick lines represent the New High Noise Model and the New Low Noise Model (Peterson, 1993).

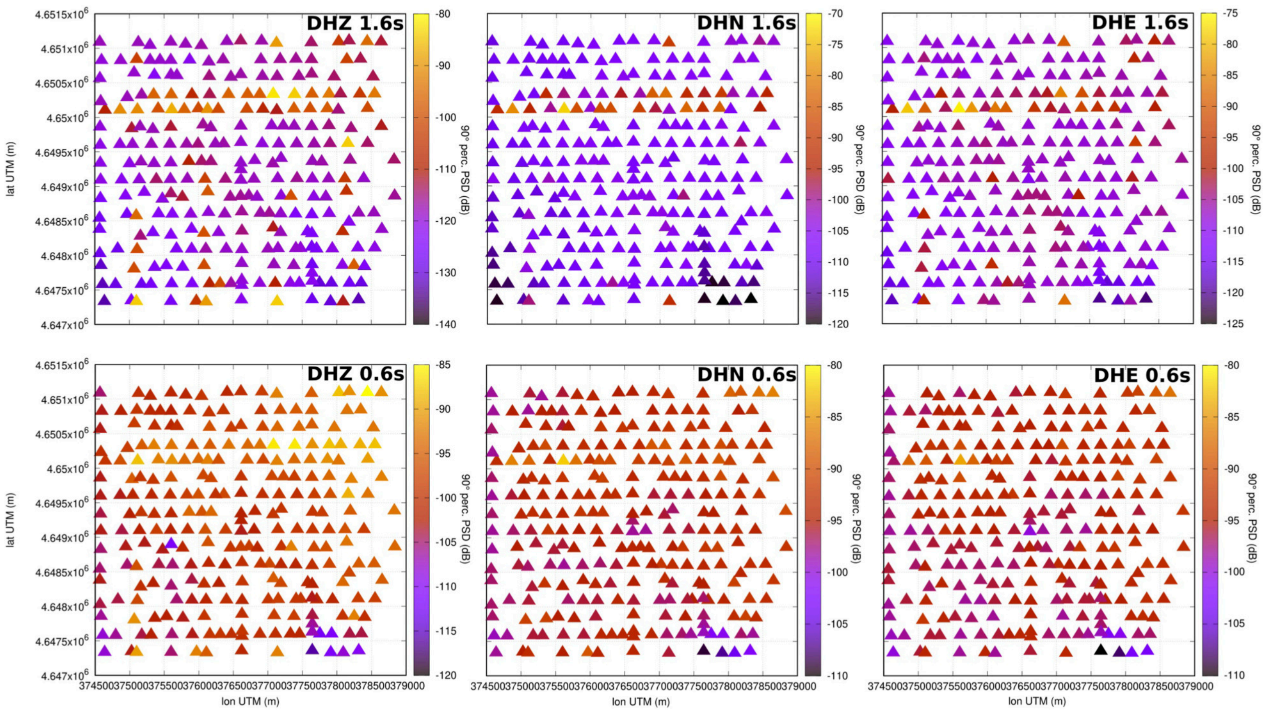

FIGURE 6
Areal distribution of the 90th percentiles at periods of 1.6 s (top subpanels) and 0.6 s (bottom subpanels), computed for the different components of the array nodal stations. The noisy stations around 4.65x10^6 on the y-axis are placed near a heavy-traffic road that is oriented W-E.

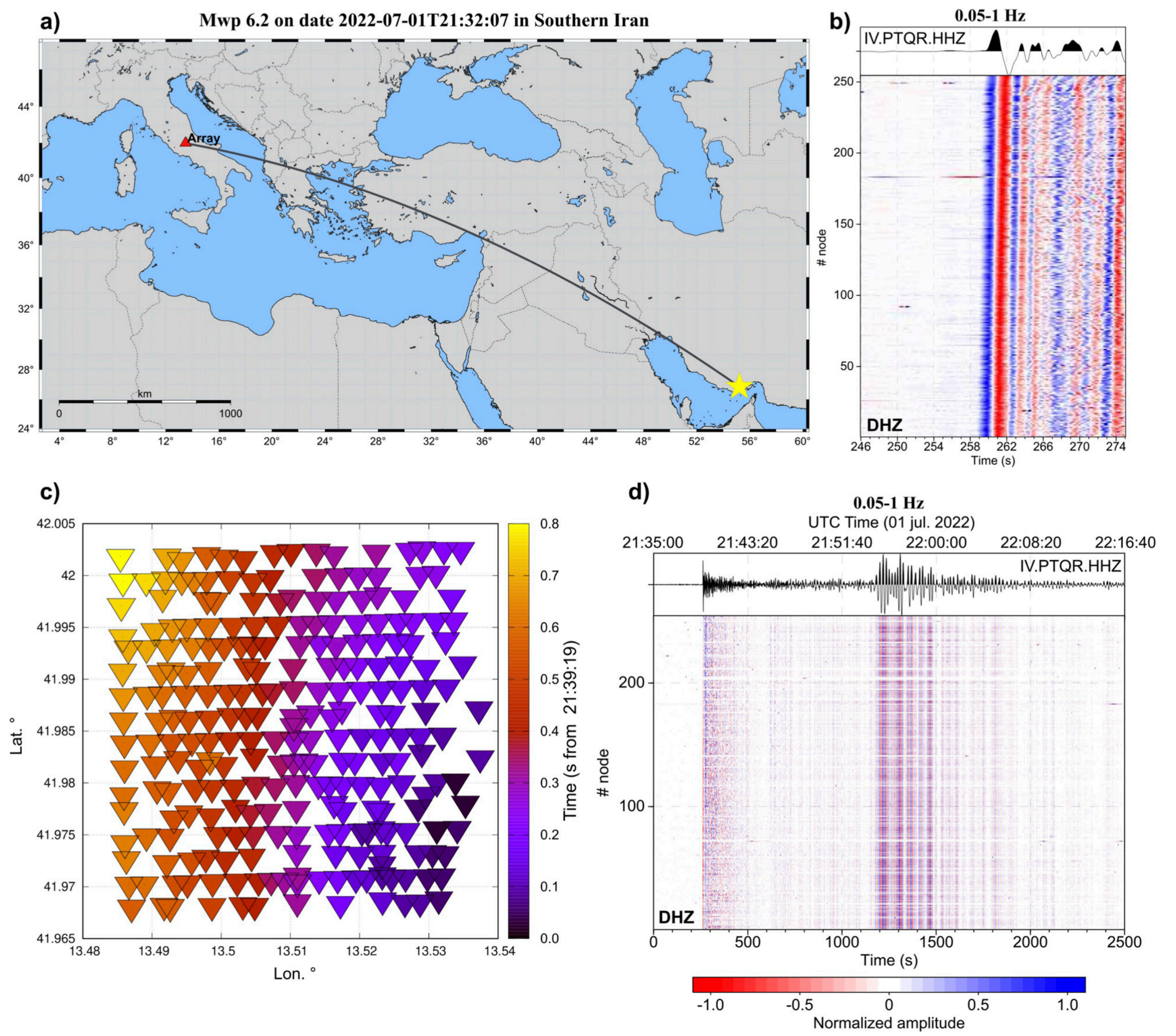

FIGURE 7
Nodal Array recordings of a teleseismic earthquake (Iran, Mw 6.2, 01-07-2022). **(a)** Map with epicenter (yellow star) and array (red triangle) positions. **(b)** Seismic signals (29 s long) around the teleseismic first arrivals recorded by vertical components of nodal stations and broad-band PTQR station of the Italian National Seismic Network located approximately 7 km to the NW of the array. The signals are corrected for instrumental response and then filtered in the 0.05–1 Hz frequency band. For nodes, the normalized amplitudes are represented in color scale with signals organized by assigning a progressively increasing number (# node) based on the epicentral distances. **(c)** Spatial distribution of the picked first arrival times at the different nodal stations. The nodes (triangles) are colour scaled according to the picked times. **(d)** Similar to **(b)** but showing 2500 s of recorded data.

3.3 Single stations noise measurements

The single-station survey aimed at collecting complementary ambient noise data to investigate the fundamental resonance frequency in the eastern, central, and southwestern sectors of the FB (Figure 8). In the eastern sector, the measurement points align along two profiles that cross from east to west strong geological heterogeneities across the San Benedetto Fault (points FUN1-FUN7 and FN14-FN16) and the Bacinetto depocenter (points FUN8-FUN10 and FN11 - FN13). The southern profile matches the HR seismic line SB (Figure 1A). The measurement points FUC1 – FUC9 and FC10 - FC25 are located within a squared area of approximately $25\ km^2$ that includes the nodal array. Several measurements were carried out close to the Trasacco Fault and along the HR seismic lines T1 (FUC1 – FUC3) and T2 (FUC11 and FUC15) (Figure 1A). The westernmost measurement was performed close to the Luco dei Marsi Fault, that is a NE-dipping normal fault hypothesized by some authors along the south-western margin of the basin (Figures 1A, 2B) (Giraudi et al., 1988; Galadini and Galli, 1999; Patruno and Scisciani, 2021).

The field activity was carried out from 21st to 24th June 2022 by using a LE3D/5s seismometer coupled with a Reftek-130 datalogger for a total of 42 recording sites (Figure 8). The mean duration of each measurement was around 1 h. The instrument was set at

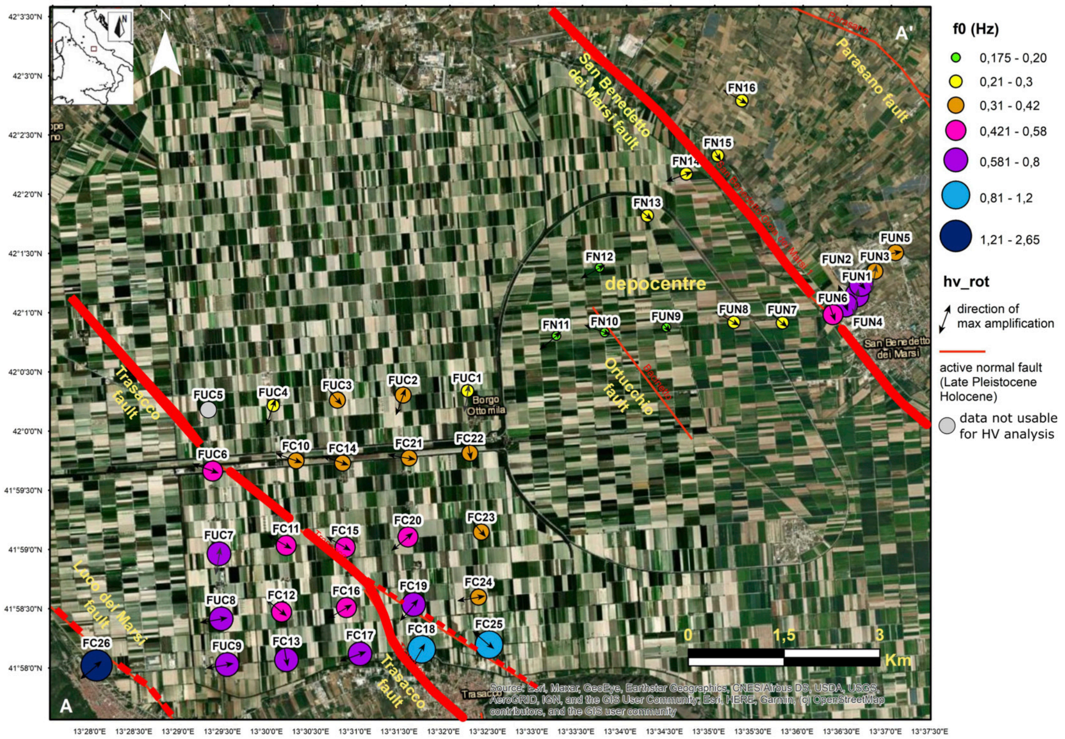

FIGURE 8
Satellite image from Google Earth Pro (https://www.google.com/earth/) with positions of single-station noise measurements. The map shows the resonant frequency (f_0) for each site indicated with coloured circles of different size depending on the f_0 values. The black arrows indicate the direction of maximum amplification. The thick red lines denote the San Benedetto and Trasacco fault traces reported by Faure Walker et al. (2021).

the sampling frequency of 100 Hz with gain 32. Ambient noise data were processed to compute horizontal to vertical spectral ratio (Nakamura, 1989) to detect the fundamental resonant frequency at each site. The analyses were performed by using the Geopsy software (www.geopsy.org): signals were windowed in time series of 60s length (cosine taper 5%) and the anti-trigger tool was used to remove transient signals. For each time window, amplitude spectra were processed using the Konno and Ohmachi (1998) smoothing filter and setting the bandwidth coefficient b = 20. Spectral ratios were computed on each selected time window, and a geometrical mean (and standard deviation) of the H/V ratios was provided. To detect preferential direction of amplification, directional H/V spectral ratios were computed considering the same time windows used for the H/V analysis. The direction corresponding to the maximum ratio is indicated through an arrow in Figure 8.

4 Results and discussions

4.1 Active seismic surveys

We present a stack section for each seismic profile, obtained using a preliminary processing flow, with the preliminary aim of illustrating data quality in terms of reflectivity, resolution, and maximum investigation depth. We then report initial results that provide new insights into the basin's structure and active faults. The preliminary processing flow is summarized in Supplementary Table S1 and does not include migration and deconvolution, which are required for detailed stratigraphic and structural interpretations of complex tectonic basins such as the FB.

The three profiles (SB, T1 and T2) display good quality in terms of reflection amplitude, continuity, and resolution (Figures 9, 10). The investigation depth allows imaging of the entire basin infill and of the upper part of the Meso-Cenozoic substratum.

Profile SB yields a very-high resolution image of the basin stratigraphy (Figures 9, 10A). Strong reflectivity characterizes the Bacinetto depocenter with high-to moderate-amplitude, continuous, and high-frequency reflectors extending from the near surface down to ~800–1100 m TWT. At greater depths, discontinuous reflectors remain visible down to 1400–1600 ms TWT. The San Benedetto Fault is clearly imaged between 3300-3600 m along the profile (Figure 9). The basin infill thickness increases sharply from 150 to 200 ms TWT in the footwall to ~1050–1100 ms TWT in the hangingwall. A shallow disrupted zone between 3300-3700 m (<200 ms TWT) mark the main fault zone, consistent with the fault trace reported in published structural maps (Faure Walker et al., 2021; Cavinato et al., 2002; Patruno and Scisciani, 2021).

Regarding data resolution, we estimated the vertical separability across different time intervals using the dominant frequency and the Root-Mean-Square (RMS) velocity derived from NMO velocity analysis. Resolution, calculated following the commonly adopted ¼ wavelength criterion, is high within the continental infill,

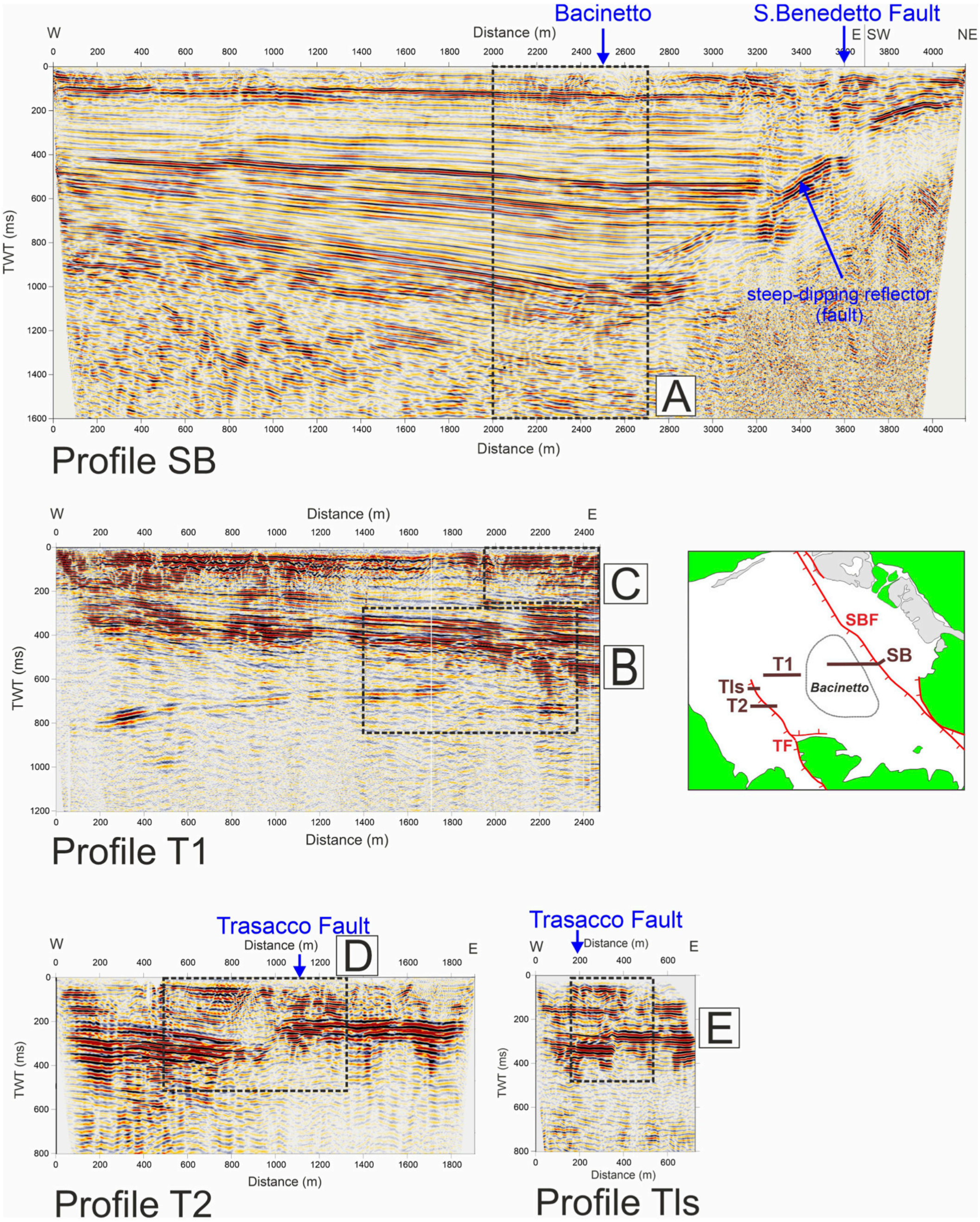

FIGURE 9
Stack sections determined for the four seismic profiles. Labelled black-dashed rectangles from **(A–E)** bound the zoomed portion of the sections in Figure 10. Blue arrows highlight the intersection of the seismic lines with the fault's traces reported by Faure Walker et al. (2021). The inset map shows the Fucino Basin, the position of the 4 HR profiles, the traces of San Benedetto Fault (SBF) and Trasacco Fault (TF), and the Bacinetto depocenter. The pre-Pliocene geological units are shown in green, the Upper Pliocene - Lower Pleistocene continental deposits are shown in grey, Lower Pleistocene - Holocene deposits in white colour.

ranging from ~3 to 7 m, in the uppermost 900–1000 ms TWT. It decreases to ~11–14 m within the Messinian units and Meso-Cenozoic rocks (Figure 10A).

Figure 11 compares profile SB with the time-migrated section of a parallel legacy profile situated ~1.5 km to the north (L1 in Figure 1), which has been interpreted differently by several authors (Patacca et al., 2008; Patruno and Scisciani, 2021; Caielli et al., 2023). This comparison highlights the markedly higher quality and resolution of SB data.

According to Patruno and Scisciani (2021), the Bacinetto depocenter has been strongly controlled since the earliest Pleistocene by the Bacinetto Fault, a structure synthetic to the San Benedetto Fault (Figure 2B). Profile SB crosses the inferred trace of this fault about 1 km south of its northern tip (Figure 2B).

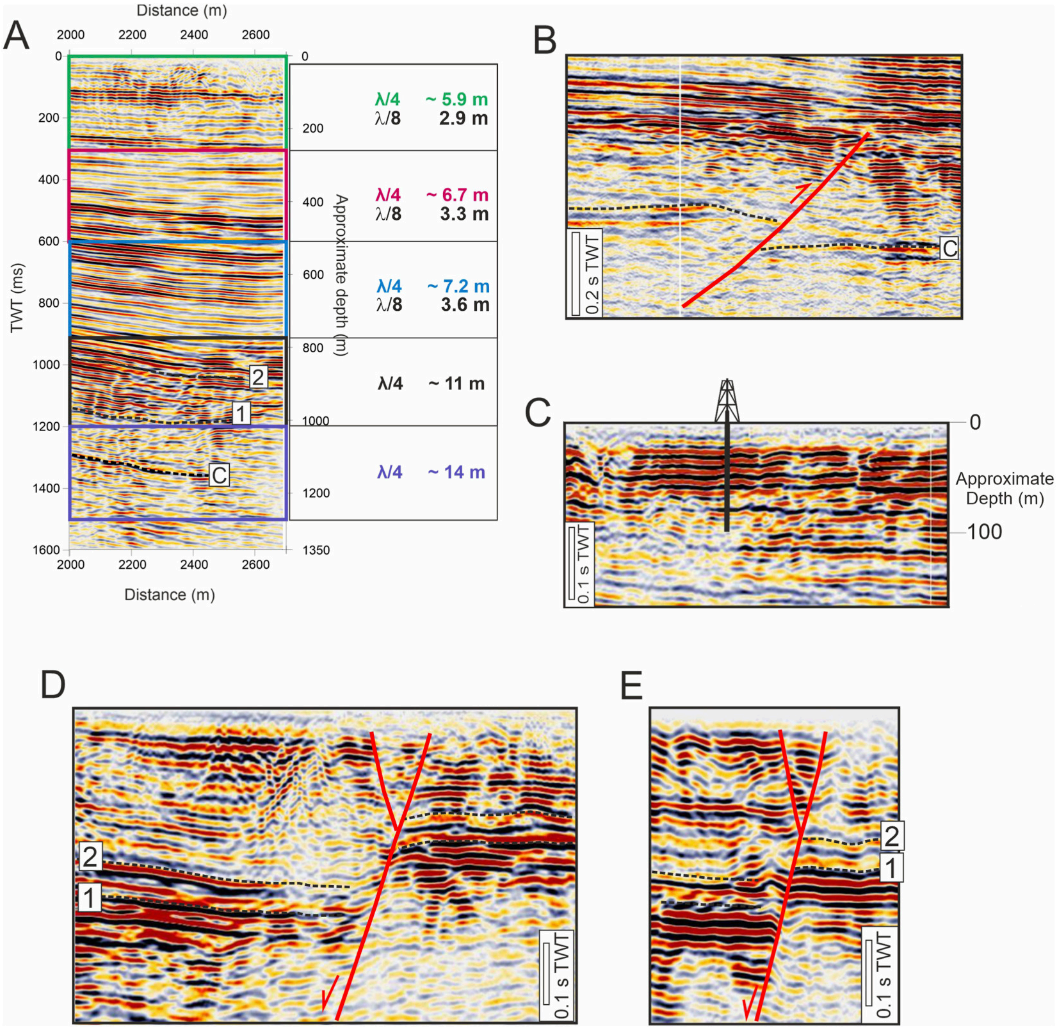

FIGURE 10
Magnification of key portions of the seismic stack sections labeled from **(A–E)** as shown in Figure 9. Main geological horizons (black-dashed lines) and faults useful to illustrate the potential of acquired seismic data are also showed: C–Meso-Cenozoic limestones, 1 - top Messinian flysch deposits, 2 – top Upper Messinian thrust-top unit (i.e., bottom of Pliocene - Quaternary continental succession). Panel **(A)** also reports the vertical resolution limits estimated for different two-way-time ranges of the profile SB computed based on the data dominant frequency and average P-wave velocities inferred from CDP-gathers velocity analysis (λ/8 and λ/4 is for very-high and high-quality data, respectively). The borehole reported in panel C is the F4-F5 scientific drilling that reached a 424 kyr-old tephra at 98 m depth (Giaccio et al., 2019). To plot the borehole onto the stack section we estimated the bottom-hole depth in TWT time by using an average P-wave velocity derived from first-arrival traveltimes.

However, our high-resolution profile reveals no significant syn-sedimentary deformation attributable to this major fault. At the 900 m mark (Figure 9), the seismic section shows only weakly warped horizons in the shallow section (0.2–0.4 s TWT) and subtle reflector truncations with a vertical separation of less than 0.02 s at depth (0.4–0.8 s TWT). Furthermore, clear evidence of growth strata is absent. These findings contrast with the interpretation of Patruno and Scisciani (2021) of a commercial seismic profile located 900 m south of profile SB (Figure 2B). They reported truncated horizons with vertical separations of 0.1–0.2 s between 0.4 and 0.8 s (TWT), a thick syntectonic wedge of Lower-Upper Pleistocene continental deposits, and a cumulative throw of the Bacinetto Fault on the order of 0.5 s (TWT).

In contrast, prolonged syn-sedimentary activity of the San Benedetto Fault within the Bacinetto is clearly documented along profile SB by: (i) gently eastward-dipping divergent reflectors towards the fault, (ii) well-developed growth strata, and (iii) a marked thickening of the continental infill in the hangingwall (Figure 9).

Seismic facies are defined by coherent reflectors with high-to-medium amplitude and very-high continuity, typical of lacustrine environments (Strecker et al., 1999), with possible fluvio-lacustrine deposits at the base. These deposits are ~1050–1100 ms TWT thick, corresponding to 850–900 m using an RMS velocity of 1700 m/s. Published estimates of the thickness of Upper Pliocene to Recent lacustrine and fluvial deposits in this sector of the Bacinetto are 900 ms in Cavinato et al. (2002), 1450–1500 ms in Patruno and Scisciani (2021), and approximately 1000 ms TWT in Caielli et al. (2023). Our results based on higher resolution data closely match with the latter interpretation.

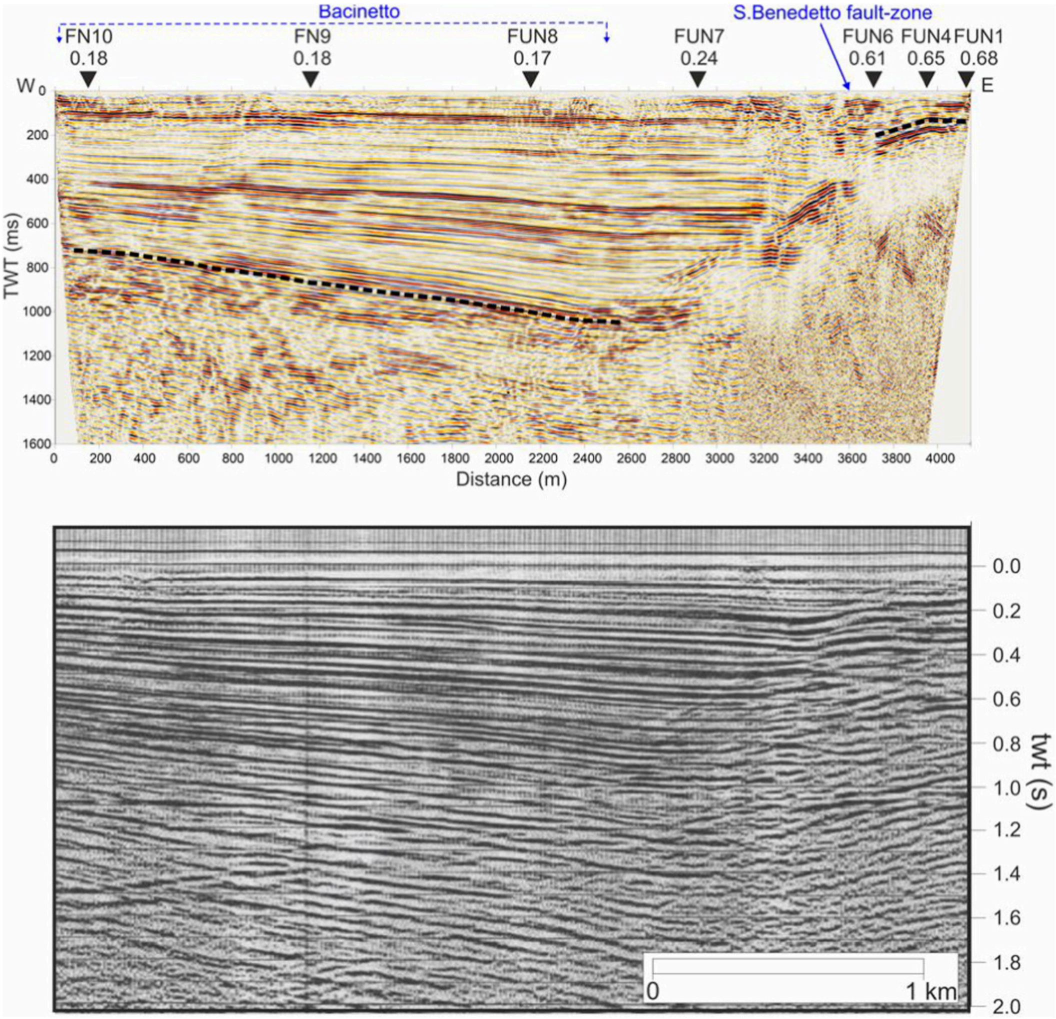

FIGURE 11
The stack section of the high-resolution profile SB is compared with the time-migrated section of the best legacy commercial profile (labelled as L1 in Figures 1, 2). This time-migrated profile was published by Patacca et al. (2008) and Patruno and Scisciani (2021). It is nearly parallel to our profile SB and located 1.5 km northward. Two previous and contrasting interpretations of profile L1 are compared in the Supplementary Figure S1. The black triangles in the top section denote the location of the stand-alone seismic stations installed along the profile SB. The value of the resonance frequency (f_0) for each site is also reported. The black-dashed line is the bottom of the Late Pliocene - Pleistocene lacustrine and fluvio-lacustrine basin infill.

In the central sector of the basin, the profile T1 reaches the exploration depth of approximately 800 ms TWT and clearly images the top of the Meso-Cenozoic carbonates. The top of the limestone unit is folded by a blind thrust-fault that appears to die out within the Messinian flysch strata (Figures 9, 10B). Seismic horizons gently dip eastward, and the thickness of the basin infill increases eastward from ~300 to 400 ms TWT.

To the east, the shallow portion of the seismic section (<150–200 ms TWT) exhibits clear and continuous reflectors. This time interval corresponds to the depth range investigated by the F4-F5 scientific drillings (Giaccio et al., 2019) (Figure 10C). At the drilling site, we estimate a dominant data frequency of the seismic section of about 70 Hz, while first-arrival traveltimes in the 0–600 m offset range indicate P-wave velocities gradually increasing from 900 to 1400 m/s with depth (Supplementary Figure S2). These values correspond to a high vertical resolution in the order of 3–5 m. Given this high resolution, which may improve further after advanced data processing, shallow reflector horizons could be tied to dated layers in the borehole in a future comprehensive study.

In the southern-western sector of the basin, profile T2 images the Trasacco Fault (Figures 9, 10D). The fault location along this profile is consistent with literature data (Cavinato et al., 2002; Patruno and Scisciani, 2021; Faure Walker et al., 2021) (Figures 2A,B). Normal faulting produces a clear, single step in the substratum and a corresponding sharp thickening of the basin infill to the west. Evidence for syn-sedimentary activity includes growth strata, back-tilted reflectors, and disrupted zones. The vertical separation of the top substratum is 100–110 ms TWT, that corresponds to 50–65 m assuming an average P-wave velocity of 1000–1200 m/s for the infill (see the results of surface-wave dispersion curves inversion for the preparatory array described in Section 4.2). The fault-zone structure is relatively simple: a single W-dipping fault cuts the basin substratum and is paired with a minor antithetic splay that displaces the shallow sediments. At the eastern edge of the T2 profile, the depth of the base of the continental infill in the fault footwall is approximately 180 ms TWT. Comparing this to profile T1, which shows the bottom of the continental sequence at 300 ms TWT (Figure 9), emphasizes the thickening of the continental fill and the deepening of the substratum in the north-east direction, consistent with previous subsurface models (Cavinato et al., 2002; Patruno and Scisciani, 2021).

The land-streamer Tls profile (Figure 10E) reaches an exploration depth of approximately 600 m TWT. Relative to the dense, wide-aperture lines T1 and T2, this profile exhibits weaker reflectivity in the deep part (>400 ms TWT), and lower data resolution (i.e., lower dominant frequency). This reduction in quality is an effect of lower CMP fold (24 instead of 72), shorter geophone array (235 m instead of 1435 m), and weaker coupling of both geophones and sources. Indeed, the vibroseis source operated on a paved embankment, rather than the flat, unpaved roads used for T1 and T2. Nevertheless, the Tls profile successfully images the basin stratigraphy and clearly detects the Trasacco Fault, 250 m to the east of the fault trace reported by Faure Walker et al. (2021). The fault-zone structure is very consistent with that imaged by profile T2 to the south. The profile Tls firmly constrains the fault location toward the north. This is in fair agreement with Faure Walker et al. (2021) and Cavinato et al. (2002), whereas it contrasts with the model of Patruno and Scisciani (2021) (see Figures 2A,B). These authors place the main SW-dipping fault segment approximately 1000 m east of the fault detected by seismic line Tls and in correspondence of the westernmost portion of the seismic line T1 (Figure 2B), which, conversely, shows no evidence of faulting.

The results from this survey test document the effectiveness of our land-streamer-vibroseis system for the imaging of shallow basins and faults (<500 m depth). We remark that the land streamer acquisition was highly cost-effective compared to the conventional profiling using a fixed array of receivers that is rolled along the line, because it requires fewer field operators and allows for faster data acquisition covering large areas. On the other hand, land streamer acquisition poses rather restrictive logistical conditions, specifically requiring straight and long paved roads, and it significantly interferes with road traffic.

From a methodological perspective, our results have general implications for the seismic exploration of continental basins. In the last 2 decades, numerous seismic surveys were carried out in fault-controlled Quaternary basins across the Apennines with acquisition procedures similar to those adopted in the FB (Bruno et al., 2025; and references therein). The seismic sections presented here provide the best images of an Apennine tectonic basin ever published in terms of resolution and exploration depth. For comparison, Villani et al. (2024) recently conducted a survey in the inhabited Campo Felice basin. They obtained seismic migrated sections of quality ranging from fair (in areas of coarse clastic sediments like moraine, slope breccias and alluvial fans) to good (for fluvio-lacustrine deposits). The exploration depth reached in Villani et al. (2024) was 400–500 m and the vertical resolution was between 8-12 m (<250–300 m depth) and of 12–25 m (>300 m depth). A comparable penetration (500–600 m depth) and vertical resolution (12–30 m) characterize seismic profiles collected inside the Castelluccio basin filled by both coarse clastic and lacustrine deposits (Villani et al., 2021).

Comparison of the Fucino seismic profiles with those acquired in other active extensional basins in the Apennines and globally, such as the Basin and Range province (Stephenson et al., 2012; Stephenson et al., 2013; Bruno et al., 2017), eastern California (Gold et al., 2020), and southeast Spain (Haberland et al., 2017) indicates that near-surface conditions play a key role in collecting high quality shallow reflection data through the source-soil coupling and effective propagation of reflected waves. These conditions govern both the vibroseis-soil coupling and the effective propagation of reflected waves. Specifically, vibroseis-soil coupling is excellent on the consolidated, fine-grained soils, characteristic of the Fucino plain's unpaved roads. Seismic penetration is high for saturated, clay-rich lacustrine sediments, but poor for coarse-grained deposits (such as alluvial fans, slope debris and alluvia), which are known to cause strong scattering (e.g., Bruno et al., 2022). Additionally, measurements of seismic attenuation in saturated sediments show that the quality factor Qp can be significantly greater for cohesive, clay-rich sediments than for granular, coarse sediments (Vardi et al., 2012). Notably, the excellent imaging achieved in the Fucino survey, both in terms of data resolution and exploration depth, was rather unexpected during the project design considering the high level of anthropogenic high-frequency noise in the plain (Figure 5). The Fucino experiment thus demonstrates that near-surface lithological conditions must be considered carefully when designing a high-resolution seismic survey. In particular, saturated fine-grained soils in the near-surface are a crucial element for successful application of shallow reflection imaging techniques.

4.2 Preparatory nodal arrays and single-stations noise measurements

Ambient noise data recorded during the two preparatory experiments provide insights regarding the performance of seismic nodes in a deep basin characterized by low resonance frequency.

For the larger preparatory array (Figure 12), the peaks of the H/V curves show a clear spatial trend of the fundamental resonance frequency (f_0). Moving from the SW corner to the NE corner, f_0 decreases from 1.5 Hz to 0.6 Hz indicating a deepening of the basin substratum, consistent with the expected geometry moving from the southwestern margin toward the basin centre (Figure 2A). Due to its limited spatial aperture, the smaller preparatory array does not resolve a significant shift in the H/V frequency peaks, which are quite consistently observed at 0.7 Hz (Figure 12).

A high-resolution beamforming (f-k) array analysis (Wathelet et al., 2018) performed on three-component data recorded by the two preparatory arrays shows clear surface-wave dispersion curves (Supplementary Figure S8). Through the Geopsy software (Wathelet et al., 2020), the bigger preparatory array measured a Rayleigh-wave dispersion curve in the frequency range 0.8–2 Hz. The smaller array captured Rayleigh dispersion from 2 to 20 Hz, where is evident the role played by higher modes. The smaller preparatory array was also able to depict a Love dispersion curve from 2 to 10 Hz, with apparent velocity ranging from 180 to 100 m/s (Supplementary Figure S8).

The vertical component data of both arrays were also processed to compute Cross-Correlation (CC) functions (Vassallo et al., 2019).

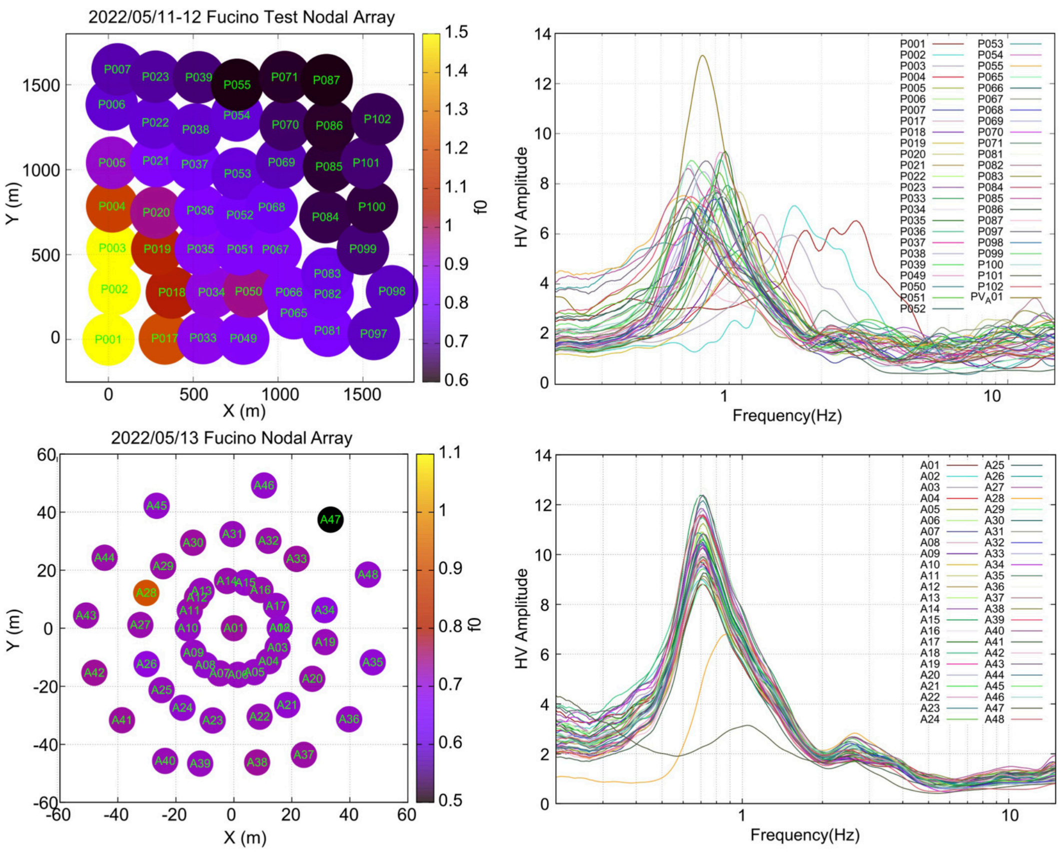

FIGURE 12
H/V curves computed by processing data of the preparatory arrays. Top and bottom panel refers to the bigger and smaller array, respectively. The distributions of f_0 values from the H/V peaks are in the left map, with the colour scale proportional to the f_0 value. The average H/V ratios for each node are overlaid on the right. For the smaller array, nodes A47 and A28 were not properly working.

We used the one-bit normalization and spectral whitening (Bensen et al., 2007), and the CC functions were computed for each station pair (Supplementary Figure S9). The dispersion curves were estimated by a phase-weighted stack velocity analysis (Schimmel and Paulssen, 1997) and were found highly consistent with the previous ones obtained from the beamforming analysis for the Rayleigh wave.

Given the good agreement between results of f-k and CC analysis, to get a first inversion results for the experimental dispersion curves, we performed a joint inversion of Rayleigh and Love wave dispersion obtained from both arrays, using the Dinver tool of Geopsy (Wathelet et al., 2020). The average H/V spectral ratio from the smaller array was incorporated in the inversion, as a proxy of Rayleigh-wave ellipticity. Because the area covered by the two arrays is relatively large and a spatial variability was observed in the H/V curves of the large preparatory array, the resulting velocity models derived from the joint inversion should be considered reliable only as a first-order approximation. The models resulting from the joint inversion of dispersion curves and Rayleigh-wave ellipticity (Figure 13), show three main seismic velocity contrasts at approximate depths of 50 m, 180 m, and 700–800 m. The shear-wave velocity (Vs) increases from about 230 m/s to 520 m/s across the first velocity contrast, and from 520 m/s to about 1300 m/s across the second contrast. For the less resolved deeper contrast, Vs. increases to more than 2000 m/s. The main shallow interface from the inversion, at a depth of approximately 50 m, is within the continental fill and may correspond to a transition from fine-grained lacustrine soils to coarser fan deposits. The second interface can be related to the top of the pre-Pliocene basin substratum (i.e., Messinian deposits), which is known to lie between 100 and 200 m depth in this area (Figure 2A). This is also supported by P-wave velocities (Vp) in the 2300–3000 m/s range (Figure 13). The deeper interface, at a depth of about 800 m, with Vs > 2000 m/s and Vp > 4500 m/s can be related to the top of the Meso-Cenozoic carbonates (Cavinato et al., 2002; Caielli et al., 2023).

The analysis of data collected by the Trasacco large-scale nodal array is underway. Here, we present initial results for several nodes that were co-located with a stand-alone seismic station (Reftek-130 datalogger equipped with a LE3D/5s velocimeter; see Section 3.3). The objective was to examine resonance frequency trends in specific sectors of the array and to compare results obtained using two different instrumentation types, which recorded data over very different time spans (approximately 1 hour for the stand-alone seismic stations versus approximately 20 days for the nodes).

The spectral analysis for the nodal array data was performed using the HVNEA software (Vassallo et al., 2022), which allows automated computation of spectral ratios from long-term seismic

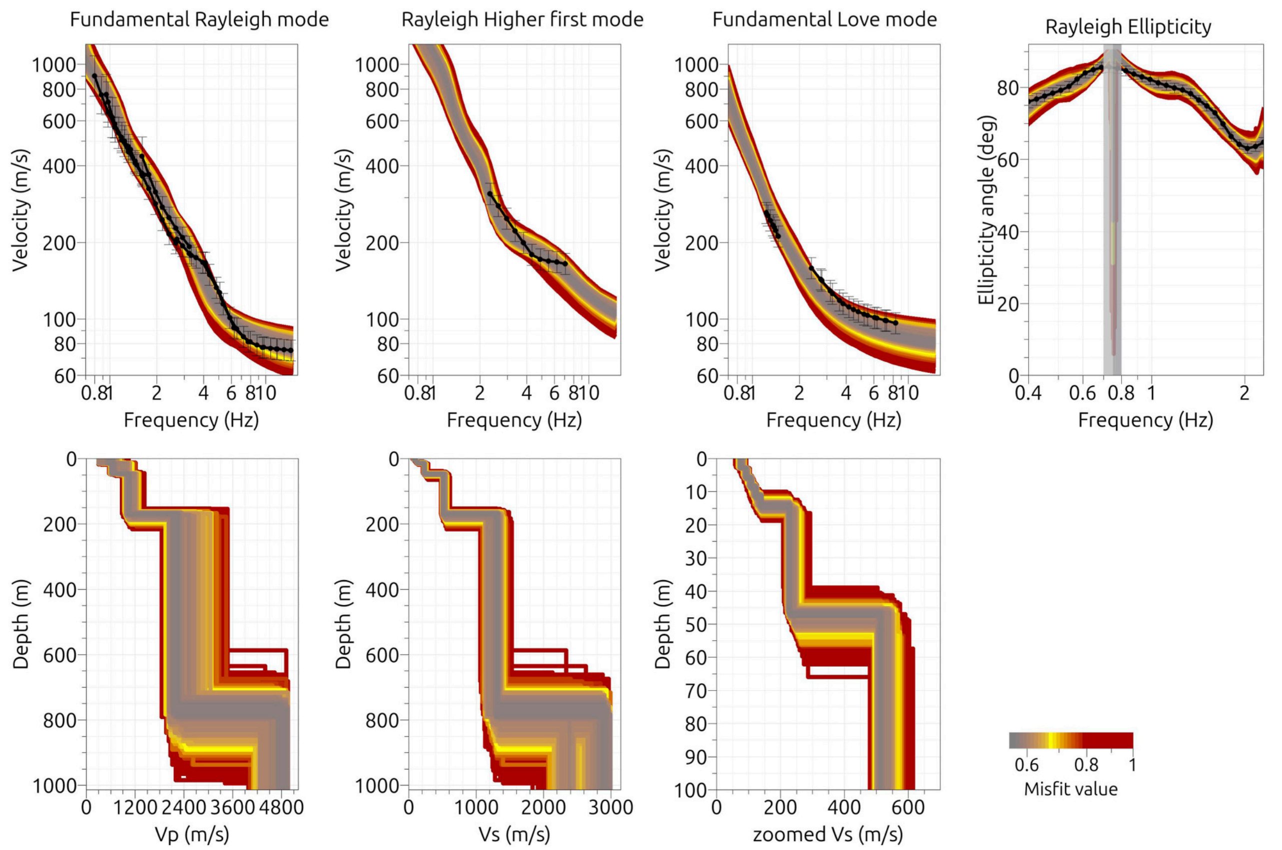

FIGURE 13
Inversion results of surface-wave dispersion curves for the preparatory arrays. The experimental dispersion curves (black curves) were obtained through f-k and cross-correlation analyses applied to both the bigger and smaller preparatory arrays. The H/V noise spectral ratio, from the smaller array, was also used as signed Rayleigh-wave ellipticity in the inversion procedure. The bottom panel shows the resulting P-wave and S-wave velocity models, including a zoomed Vs. profile within the uppermost 100 m. The suite of inverted models follows the misfit color scale, with the misfit representing the degree of mismatch between experimental and theoretical curves.

recordings spanning weeks/months or even years. To compute H/V spectral ratios with HVNEA, the continuous recordings were segmented into 3600 s time windows. For each segment, the geometric mean of estimates obtained from 60-second sub-windows was calculated, after applying the Konno and Ohmachi (1998) smoothing filter with the bandwidth coefficient set to b = 20. The final H/V curve representing each site was then derived as the geometric mean of the hourly curves.

Figure 14 presents the H/V curves for nodal stations N047, N111, N175, and N239, which are located along the northern edge of the array (white dots in Figure 3). These results are compared with the H/V spectral ratios derived from nearby stand-alone seismic stations (red stars in Figure 3). For sites N111, N175, and N239, the two types of instruments exhibit good consistency in both the frequency and amplitude of the H/V peaks, although the nodal data tend to highlight these peaks more distinctly and with lower uncertainties, likely due to the longer duration of the records. In contrast, at site N047, the agreement deteriorates below 0.7 Hz, where the H/V curve for the stand-alone seismic station rises sharply with decreasing frequency, while the nodal station displays a spectral shape more consistent with that observed at the other sites. This discrepancy may be attributed to transient disturbances, likely anthropogenic, affecting the shorter, one-hour recording at the seismic station FUC5 (Figure 8), thereby hindering the H/V estimate. From west to east, f_0 decreases from 0.5 Hz (site N047) to 0.4–0.5 Hz (sites N111 and N175), and then to approximately 0.3 Hz (site N239). This spatial trend is consistent with the eastward thickening of the Pliocene-Quaternary sediments imaged by the HR seismic line T1, which runs along the northern side of the array (Figures 1A, 9).

A further comparison between the H/V spectral ratios calculated for five nodal stations and five nearby seismic stations equipped with Lennartz LE3D/5s velocimeters is shown in the Supplementary Figure S10. Each couple of H/V curves displays prominent peaks at nearly identical frequencies between 0.45 to 0.75 Hz, in agreement with the comparison reported in Figure 14.

H/V spectral ratios were computed for three nodal stations (N177, N193, and N176N) located in the southeastern sector of the array, close to the Trasacco Fault (Figure 3). The goal was to assess whether nodal data allows detecting this intra-basin, hidden fault. Despite being situated less than 300 m apart, the three sites display different spectral peaks (Figure 14). The H/V peak at station N177, located in the hangingwall of the fault, occurs at 0.7 Hz, while the peak at station N176N, on the footwall, is around 0.9 Hz.

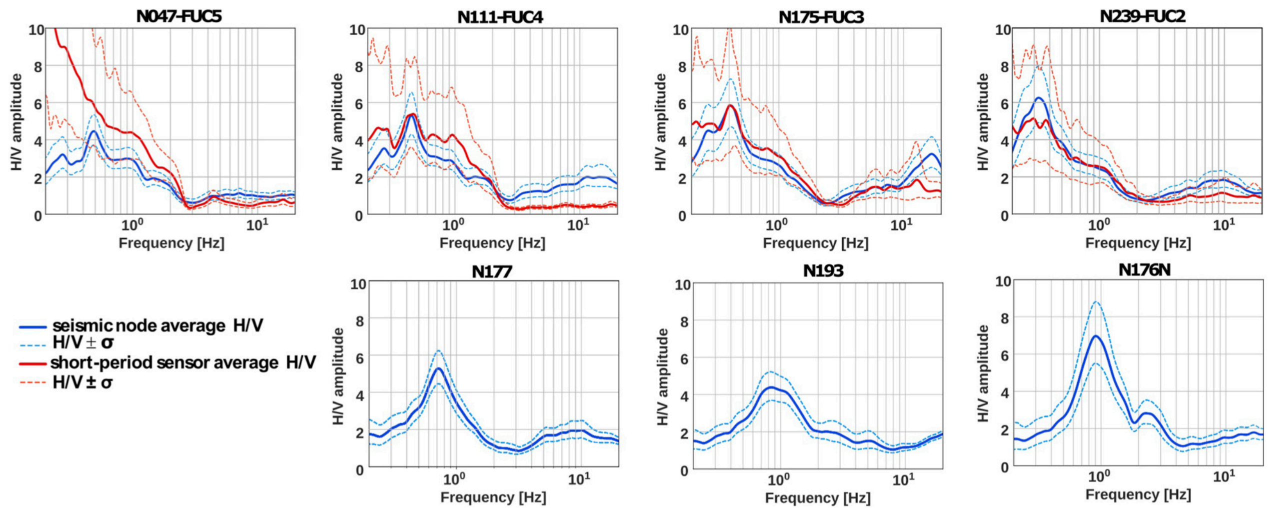

FIGURE 14
Ambient noise H/V curves estimated at seven nodes of the Trasacco array. Location of these nodes is highlighted in Figure 3. Nodes N047, N111, N175, and N239 are aligned along the northern edge of the array. The H/V curves for node stations (blue lines) are compared to those estimated for co-located stand-alone seismic stations FUC2 to FUC5 (red lines). Node stations N177, N193 and N176N are located across the Trasacco fault-zone: N176N in the fault footwall, N193 above the presumed fault, N177 in the fault hangingwall.

Station N193, positioned between the other two nodes and directly above the presumed fault trace, exhibits a broader spectral peak encompassing those of the adjacent stations.

Assuming an average S-wave velocity of 500 m/s for the fill sediments, consistent with results obtained by the preparatory arrays (Figure 13), the difference in f_0 for sites N176N and N177 corresponds to a thickening of the basin fill across the fault in the order of 50 m, consistently with results of HR seismic profile T2. This value is comparable to the thickening of the infill across the fault previously reported by Cavinato et al. (2002) at the southern edge of the basin (Figure 2A).

These analyses indicate that ambient noise data recorded by the Trasacco large-scale array can effectively be used in a next focused work to map small-scale spatial variations of f_0 across the FB, particularly where thick sequences of fine-grained sediments are responsible for resonances below 1 Hz, and to map rapid depth changes of the substratum caused by faults.

Single-station ambient noise measurements confirm the results derived from the nodal arrays and reveal the high variability of the resonance frequency across the whole basin (Figure 8). At first sight, a general decrease in f_0 is observed moving from the margin of the Fucino plain toward the Bacinetto depocenter (Figure 15). In the eastern sector of the basin, the southern transect shows the resonance frequency f_0 around 0.3–0.4 Hz to the northeast of the San Benedetto Fault (sites FUN3 and FUN5 in Figure 8), increasing to 0.6–0.7 Hz near the fault trace (FUN1, FUN2, FUN4 and FUN6), and then decreasing westward to 0.24 Hz (FUN7) and further to 0.17–0.18 Hz in the fault hangingwall (FUN8, FN9 and FN10). The f_0 trend well correlates with the variation in thickness of the Pliocene-Quaternary lacustrine sediments across the fault, as clearly imaged by the co-located seismic profile SB (Figure 11). This profile indicates the bottom of continental deposits at 150–200 ms TWT just east of the fault trace (sites FUN1, FUN4 and FUN6) and between 800-1000 ms TWT under the Bacinetto depocenter (FUN8, FN9 and FN10). Station FUN7 (f_0 = 0.24 Hz) is located above the fault plane. Consistent values of f_0 are reported by Cara et al. (2011) for nearby sparse sites (sites LP05, LP06 and MTE).

The northern transect (site FN13 to FN16) exhibits f_0 values between 0.2-0.3 Hz, with no relevant variations across the San Benedetto Fault (Figure 8). In all these measurements along the two transects, there is no clear preferential direction of amplification.

The difference in f_0 trend between the two transects across the fault likely reflects spatial variations in the thickness of the continental fill between the eastern and north-eastern sectors of the basin. This is supported by the contour map of the base of the Upper Pliocene - Pleistocene continental deposits shown in Figure 2A (Cavinato et al., 2002). First, the map illustrates a NW-ward thickening of these deposits in the footwall of the San Benedetto Fault from 100 to 200 ms TWT (corresponding to about 100–200 m) at the southern transect to 400 ms TWT (corresponding to about 400 m) at the northern transect. Thicker footwall deposits to the north align with the lower f_0 values observed there. Then, we observe a drastic fault-related thickening of continental deposits along the southern transect, from 100–200 ms–800 ms TWT, corresponding to a jump of approximately 600–700 m. Along the northern transect, the fault-related thickening is smaller (from 400 ms to 700 ms TWT, that is a variation of ~300 m). This relatively small change in sediment thickness across the fault in the north may explain the lack of significant variation in f_0.

Sites FN10, FN11 and FN12 within the Bacinetto depocenter (Figure 8), where the continental sequence is 600–700 ms thick and mainly consists of lacustrine deposits (see Figure 2A), show low f_0 values around 0.2 Hz. In the same area, the sparse sites of Cara et al. (2011) show consistent f_0 values of 0.20–0.25 Hz.

Sites FUC1 - FUC9 and FC10 - FC25 in the southwestern sector of the basin show a general f_0 trend that decreases northward and eastward (Figure 8). The f_0 values vary from 0.6 to 1.0 Hz along

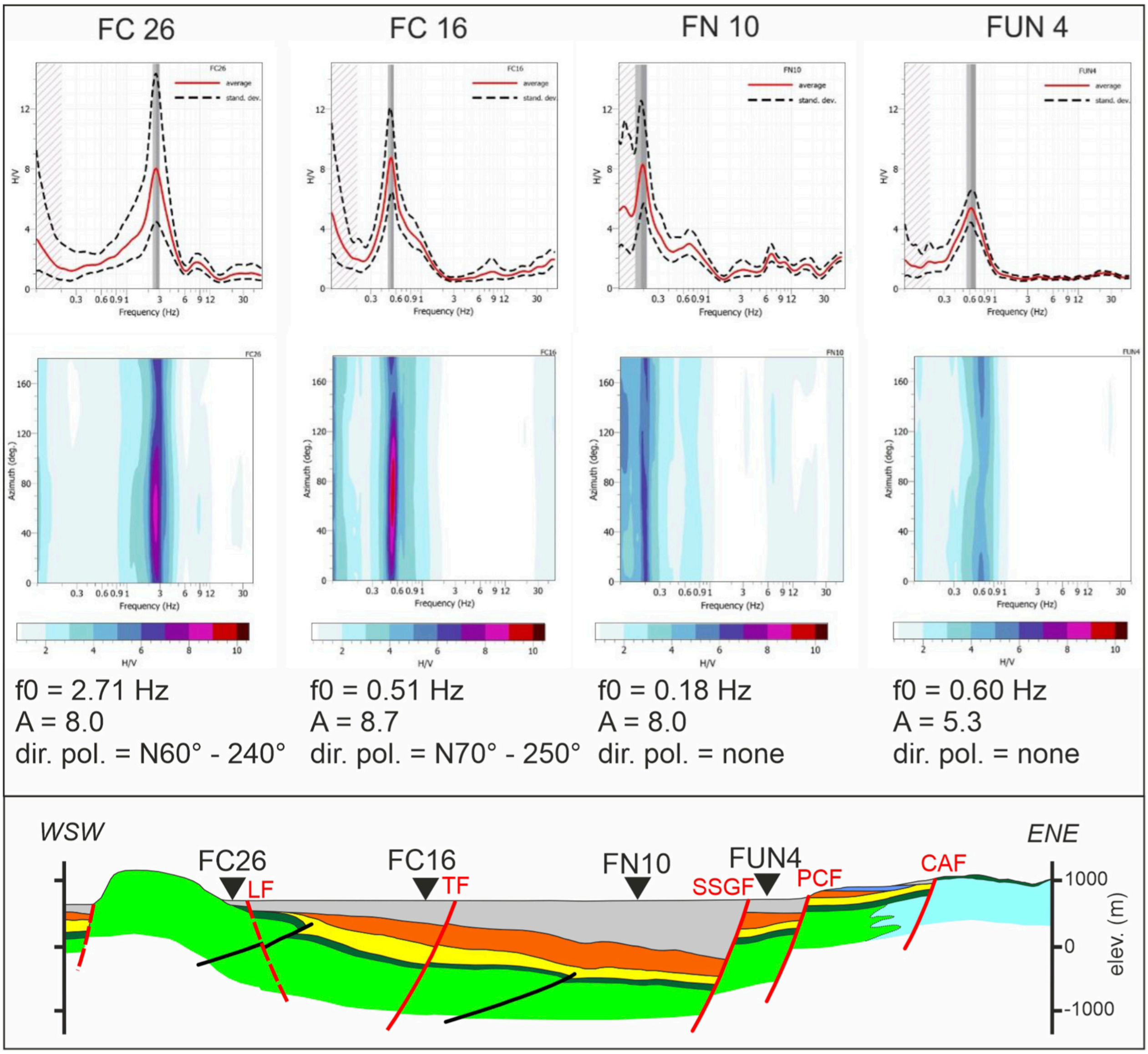

FIGURE 15
Comparison between ambient noise H/V curves and polar plots H/V estimated at four sites located at the edges and inside the Fucino Basin. The azimuthal plots are based on the ratio between the rotated mean of horizontal components (between 0° and 175°, with step of 5°) and the vertical one, with frequency for x-axis and rotational degree for y-axis. The color scale is proportional to the H/V amplitude. The four sites are plotted onto a schematic geological section in the lower panel (refer to Figure 1B for the geological legend).

the south-western margin of the basin and decrease to 0.3–0.4 Hz in the north-east area, reaching a minimum value of 0.2 Hz at the northeastern edge of the survey area (site FUC1). This general trend of f_0 is consistent with the findings of Famiani et al. (2022) in the south-western margin of the basin and is directly attributed to the NE-deepening of the basin substratum, which is supported by our HR seismic profiles (Figure 9) and existing subsurface models (Cavinato et al., 2002; Patruno and Scisciani, 2021). Cara et al. (2011) also reported very similar resonance frequency values in this area (site PI04, LP03, LP02 and MIS3).

Based on the results obtained through the closely spaced nodal stations N176N, N177 and N193 described before (Figure 14), spatial variation in f_0 shown by some recording sites can be directly linked to the Trasacco Fault. At the southeastern edge of the survey area, sites FC25 and FC18 that show the highest f_0 values (around 1 Hz) are located in the fault footwall (Figure 8), where the carbonate substratum is 50–100 m deep (Figure 2A). The nearby site FC17 located to the west in the fault hangingwall, where the substratum is 150 m deep, shows a lower f_0 of 0.7 Hz. A similar trend is observed further north between sites FC19 (f_0 = 0.7 Hz) and FC16 (0.5 Hz) (Figure 8).

Furthermore, sites FUC8, FUC9, FC16, FC17, FC19 and FC20 show important directions of maximum amplification. These vary from 80° to 260° (FUC8, FUC9) to 40°/60°–220°/240° (FC16, FC17, FC19, FC20), which are nearly perpendicular to the strike of the Trasacco Fault (Figure 8).

The westernmost site, FC26, located close to the Luco Fault at the edge of the basin, highlights a f_0 of 2.7 Hz (Figures 8, 15). Here, the basin substratum is shallow (~50 m, Cavinato et al., 2002). Site FC26 also exhibits a clear direction of maximum amplification of 60°–240°, which is perpendicular to the strike of the presumed fault, thus supporting the existence of a blind structure.

5 Conclusion

With the integrated active and passive seismic surveys conducted in the Fucino plain, we successfully acquired a large quantity of high-quality seismic reflection and ambient noise data. Given the superior resolution, signal-to-noise ratio and reflectors imaging, the new seismic profiles facilitate more robust stratigraphic and structural interpretations compared to the previous conflicting models based on legacy commercial profiles (Cavinato et al., 2002; Patruno and Scisciani, 2021; Caielli et al., 2023). Our analysis indicates that the nodal data set is suitable for a detailed investigation of the spatial variations in the fundamental resonance frequency (f_0) and the basin velocity structure. Single-station H/V curves estimated on the larger-scale transects confirm the results derived from the nodal array and effectively identify the fundamental resonance across a significant portion of the basin. By comparing f_0 with subsurface models, we can refine previous interpretations of the basin's seismic response that relied on sparse recording sites (Cara et al., 2011).

Even though the processing of seismic reflection data is still preliminary and the analysis of the noise data set recorded by the Trasacco array is underway, our initial results provide new insights into the basin stratigraphy and the structure of the San Benedetto and Trasacco faults. We point out the following conclusions:

- The main Bacinetto depocenter has been controlled by the syn-sedimentary activity of the San Benedetto fault. Unlike previous geological models, we did not find evidence in the subsurface beneath the Bacinetto for either a primary synthetic fault, as proposed by Patruno and Scisciani (2021), or an antithetic fault, as proposed by Cavinato et al. (2002).
- In the Bacinetto, seismic facies and reflection terminations suggest significant long-lasting deposition of lacustrine deposits, with possible fluvio-lacustrine deposits at the base. Along the seismic profile SB, these deposits attain a thickness of 1050–1100 m TWT (corresponding to about 850–900 m). This value is consistent with the recent interpretation of legacy seismic data reported by Caielli et al. (2023), but it is much lower than the 1450–1500 m TWT hypothesized by Patruno and Scisciani (2021) for the Upper Pliocene - Pleistocene continental infill of the Bacinetto.
- In the Bacinetto, divergent reflectors and growth strata within the lacustrine infill document the prolonged activity of the San Benedetto fault during the Late Pliocene - Pleistocene.
- Along the investigated transects, the Trasacco Fault has produced a single step in the substratum, corresponding to a total estimated throw of 50–65 m, and a westward thickening of the continental deposits. The vertical separation of the substratum's top decreases northward consistently with slip tapering toward the fault northern edge.
- The location of the Trasacco Fault along profiles T2 and Tls is in good agreement with the structural maps of Cavinato et al. (2002) and Faure Walker et al. (2021), but the northward prolongation of the fault is shifted 1000 m westward relative to the model of Patruno and Scisciani (2021).
- The f_0 obtained from the H/V curves ranges from 1 to 2 Hz at the basin edges to 0.2 Hz in the central sector of the basin and in the Bacinetto depocenter.
- The spatial variations of f_0 are gradual and mimic the progressive NE-ward thickening of the low-velocity lacustrine and fluvio-lacustrine deposits (characterized by a mean Vs. < 500 m/s). Ambient noise measurements captured sudden changes in f_0 in correspondence with the San Benedetto and Trasacco faults, where their activity has caused an abrupt thickening of low-velocity sediments.

Based on the quality of the passive and active seismic data, we highlight the following general methodological points:

- Despite the high level of anthropogenic noise, we successfully collected vibroseis reflection data exhibiting remarkable signal-to-noise ratio, resolution, and exploration depth. The presence of saturated lacustrine sediments in the near-surface was crucial for acquiring good-quality data, as it facilitated optimal source-soil coupling and effective propagation of reflected waves inside cohesive, clay-rich saturated sediments.
- The H/V curves determined using nodal stations (eigen-frequency 4.5 Hz) and seismic stations (eigen-frequency 0.2 Hz) showed consistent low-frequency spectral peaks (0.2–1.0 Hz). This result documents the efficacy of short-period nodal arrays in identifying fundamental resonance frequencies via H/V spectral ratio noise analysis in deep basins, such as the Fucino, which are characterized by thick, low-velocity sedimentary successions and f_0 well below the node's eigen-frequency. The capability to rapidly deploy nodal stations and perform long-term recordings (up to several weeks) allows for robust and stable spectral H/V estimates, even in areas affected by significant anthropogenic noise. In such contexts, the ability to quickly install a dense array of nodes also facilitates the indirect reconstruction of fault geometries.
- Preliminary analyses carried out in this study indicate that the nodes are also highly effective for reconstructing shear-wave velocity (Vs.) models using array-based methods such as frequency–wavenumber and seismic noise cross-correlation. The simple and rapid deployment of a large number of nodes enables the identification of optimal time windows for array analysis, specifically those least affected by anthropogenic noise. Furthermore, they allow for repeated analyses across multiple time windows, thereby increasing the robustness of the results. These characteristics facilitate the execution of analyses suitable for the reconstruction of three-dimensional velocity models.

Data availability statement

The original contributions presented in the study are included in the article/Supplementary Material, further inquiries can be directed to the corresponding author.

Author contributions

LI: Conceptualization, Validation, Data curation, Project administration, Supervision, Methodology, Funding acquisition, Writing – original draft, Formal Analysis, Investigation. SM: Validation, Supervision, Data curation, Writing – original draft, Methodology, Formal Analysis, Investigation. GG: Formal Analysis, Validation, Data curation, Methodology, Supervision, Writing – original draft, Investigation. MV: Supervision, Methodology, Investigation, Data curation, Validation, Writing – original draft, Formal Analysis. MM: Funding acquisition, Validation, Methodology, Supervision, Formal Analysis, Project administration, Data curation, Writing – original draft, Investigation. SL: Investigation, Supervision, Writing – original draft, Formal Analysis, Data curation, Methodology, Validation. ML: Writing – review and editing, Methodology, Investigation. FV: Writing – review and editing, Investigation. SH: Writing – review and editing, Investigation. DF: Writing – review and editing, Investigation. AM: Investigation, Writing – review and editing. PM: Project administration, Funding acquisition, Investigation, Supervision, Writing – review and editing. VS: Investigation, Writing – review and editing. A'DA: Investigation, Writing – review and editing. PG: Writing – review and editing, Investigation. CB: Writing – review and editing, Investigation. RiC: Writing – review and editing, Investigation. AS: Writing – review and editing, Investigation. PR: Investigation, Writing – review and editing. AF: Writing – review and editing, Investigation. SB: Writing – review and editing, Investigation. SPi: Investigation, Writing – review and editing. GR: Writing – review and editing, Investigation. RoC: Investigation, Writing – review and editing. GB: Writing – review and editing, Investigation. SaS: Writing – review and editing, Investigation. StS: Writing – review and editing, Investigation. LR: Investigation, Writing – review and editing. PB: Writing – review and editing, Investigation. GC: Investigation, Writing – review and editing. SPo: Investigation, Writing – review and editing. LV: Writing – review and editing, Investigation. PDG: Writing – review and editing, Investigation. AR: Investigation, Writing – review and editing. DS: Writing – review and editing, Investigation. IM: Writing – review and editing, Project administration. GM: Writing – review and editing, Funding acquisition, Investigation.

Funding

The author(s) declared that financial support was received for this work and/or its publication. This work has been funded by the INGV Project Pianeta Dinamico (code C.U.P. D53J19000170001) financed by the Ministry of Education, Universities and Research (MIUR) ("Fondo finalizzato al rilancio degli investimenti delle amministrazioni centrali dello Stato e allo sviluppo del Paese", legge n. 145/2018) - Task S2 "Struttura 3D dell'Italia da analisi multidato: Sismica passiva/attiva, Prospezioni magnetiche, magnetotelluriche, elettriche, gravimetriche" Coordinators: Luigi Improta, Marco Massa, Paolo Marco De Martini, Irene Molinari.

Acknowledgements

We sincerely thank the Associate Editor Paolo Capuano and three reviewers for taking the time to review our manuscript and providing constructive feedback to improve our manuscript. Active seismic data were acquired under an agreement between INGV and Centro di Geotecnologie (CGT) of Siena University. We acknowledge support of this work via a Landmark Grant Program to INGV by Halliburton Software and Services, a Halliburton Company. We acknowledge the following laboratories for kindly providing the seismic instrumentation used in this work: INGV Laboratory "Geologia e Geotecnologie" (https://www.ingv.it/monitoraggio-e-infrastrutture/laboratori/laboratorio-geologia-e-geotecnologia); INGV Laboratory "Esito" (https://www.ingv.it/en/monitoraggio-e-infrastrutture/laboratori/laboratorio-effetti-di-sito); Laboratory of Crustal Deformation and Fluid Flow, Department of Earth Sciences, University of Geneva (https://www.unige.ch/sciences/terre/en/groups/crustal-deformation-and-fluid-flow/lab). We acknowledge Maria Basi (Director Ufficio Rischio Sismico Regione Abruzzo), C. Lobene (Mayor of Trasacco), D. Taricone (Secretarial Office of Trasacco), A. Colantonio (Coordinator Ufficio Tecnico of San Benedetto dei Marsi), P. Iannuzzi and D. Crisante (Ufficio Tecnico of Luco dei Marsi), and R. Alatari (Ufficio Tecnico of Celano) for logistical support and for providing the authorizations to perform the seismic experiments in the Fucino plain.

Conflict of interest

The author(s) declared that this work was conducted in the absence of any commercial or financial relationships that could be construed as a potential conflict of interest.

The author PG declared that they were an editorial board member of Frontiers at the time of submission. This had no impact on the peer review process and the final decision.

Generative AI statement

The author(s) declared that generative AI was not used in the creation of this manuscript.

Any alternative text (alt text) provided alongside figures in this article has been generated by Frontiers with the support of artificial intelligence and reasonable efforts have been made to ensure accuracy, including review by the authors wherever possible. If you identify any issues, please contact us.

Publisher's note

their affiliated organizations, or those of the publisher, the editors and the reviewers. Any product that may be evaluated in this article, or claim that may be made by its manufacturer, is not guaranteed or endorsed by the publisher.

Supplementary material

The Supplementary Material for this article can be found online at: https://www.frontiersin.org/articles/10.3389/feart.2026.1778360/full#supplementary-material

References

Bagh, S., Chiaraluce, L., De Gori, P., Moretti, M., Govoni, A., Chiarabba, C., et al. (2007). Background seismicity in the Central Apennines of Italy: the Abruzzo region case study. *Tectonophysics* 444, 80–92. doi:10.1016/j.tecto.2007.08.009

Bensen, G. D., Ritzwoller, M. H., Barmin, M. P., Levshin, A. L., Lin, F., Moschetti, M. P., et al. (2007). Processing seismic ambient noise data to obtain reliable broad-band surface wave dispersion measurements. *Geophys. J. Int.* 169 (3), 1239–1260. doi:10.1111/j.1365-246x.2007.03374.x

Bruno, P. P. G., DuRoss, C. B., and Kokkalas, S. (2017). High-resolution seismic profiling reveals faulting associated with the 1934 Ms 6.6 Hansel Valley earthquake (Utah, USA). *Geol. Soc. Am. Bull.* 129, 1227–1240. doi:10.1130/B31516.1

Bruno, P. P. G., Villani, F., and Improta, L. (2022). High-resolution seismic imaging of fault-controlled basins: a case study from the 2009 Mw 6.1 central Italy earthquake. *Tectonics* 41 (4), e2022TC007207. doi:10.1029/2022tc007207

Bruno, P. P. G., Ferrara, G., Improta, L., and Maraio, S. (2025). 3D high-resolution seismic imaging of elusive seismogenic faults: the pantano-ripa rossa fault, Southern Italy. *Remote Sens.* 17 (22), 3717. doi:10.3390/rs17223717

Caielli, G., Maffucci, R., de Franco, R., Bigi, S., Parotto, M., Mollica, R., et al. (2023). Fucino Basin structure revealed by the tomography and the reusing of the CROP11 seismic data. *Tectonophysics* 865, 230043. doi:10.1016/j.tecto.2023.230043

Cara, F., Di Giulio, G., Cavinato, G. P., Famiani, D., and Milana, G. (2011). Seismic characterization and monitoring of the Fucino basin (central Italy). *Bull. Earthq. Eng.* 9, 1961–1985. doi:10.1007/s10518-011-9282-2

Cavinato, G. P., Carusi, C., Dall'Asta, M., Miccadei, E., and Piacentini, T. (2002). Sedimentary and tectonic evolution of Plio–Pleistocene alluvial and lacustrine deposits of Fucino Basin (Central Italy). *Sediment. Geol.* 148, 29–59. doi:10.1016/S0037-0738(01)00209-3

Cella, F., Nappi, R., Paoletti, V., and Florio, G. (2021). Basement mapping of the Fucino Basin in Central Italy by ITRESC modeling of gravity data. *Geosciences* 11 (10), 398. doi:10.3390/geosciences11100398

Ciaccio, M. G., Mandiello, A. G., Colini, L., Battelli, A., Mele, G. R., Misiti, V., et al. (2023). Data from: Bollettino Sismico Italiano (BSI), II quadrimestre 2022. *Istituto Nazionale di Geofisica e Vulcanologia (INGV)*. doi:10.13127/BSI/202202

Cipollari, P., Cosentino, D., Esu, D., Girotti, O., Gliozzi, E., and Praturlon, A. (1999). Thrust top lacustrine-lagoonal basin development in accretionary wedges: late Messinian (Lago- Mare) episode in the Central Apennines (Italy). *Palaeogeogr. Palaeoclimatol. Palaeoecol.* 151, 149–166. doi:10.1016/s0031-0182(99)00026-7

Cosentino, D., Asti, R., Nocentini, M., Gliozzi, E., Kotsakis, T., Mattei, M., et al. (2017). New insights into the onset and evolution of the central Apennine extensional intermontane basins based on the tectonically active L'Aquila Basin (Central Italy). *GSA Bull.* 129 (9–10), 1314–1336. doi:10.1130/B31679.1

Dean, T., Tulett, J., and Barnwell, R. (2018). Nodal land seismic acquisition: the next generation. *First Break* 36 (1), 47–52. doi:10.3997/1365-2397.n0061

Di Naccio, D., Famiani, D., Liberi, F., Boncio, P., Cara, F., De Santis, A., et al. (2020). Site effects and widespread susceptibility to permanent coseismic deformation in the Avezzano town (Fucino Basin, Central Italy): constraints from detailed geological study. *Eng. Geol.* 270, 105583. doi:10.1016/j.enggeo.2020.105583

Famiani, D., Cara, F., Di Giulio, G., Vassallo, M., and Milana, G. (2022). Detection of hidden faults within the Fucino basin from single-station ambient noise measurements: the case study of the Trasacco fault system. *Front. Earth Sci.* 10, 937848. doi:10.3389/feart.2022.937848

Faure Walker, J., Boncio, P., Pace, B., Roberts, G., Benedetti, L., Scotti, O., et al. (2021). Fault2SHA Central Apennines database and structuring active fault data for seismic hazard assessment. *Sci. Data* 8 (1), 87. doi:10.1038/s41597-021-00868-0

Galadini, F., and Galli, P. (1999). The Holocene paleoearthquakes on the 1915 Avezzano earthquake faults (central Italy): implications for active tectonics in the central Apennines. *Tectonophysics* 308 (1-2), 143–170. doi:10.1016/s0040-1951(99)00091-8

Galadini, F., and Messina, P. (1994). Plio-Quaternary tectonics of the Fucino basin and surrounding areas (Central Italy). Giorn. *Geol.* 56, 73–99. Available online at: https://hdl.handle.net/20.500.14243/256289.

Galadini, F., Galli, P., and Giraudi, C. (1997). Geological investigations of Italian earthquakes: new paleoseismological data from the Fucino Plain (Central Italy). *J. Geodyn.* 24 (1-4), 87–103. doi:10.1016/s0264-3707(96)00034-8

Galli, P., Galadini, F., and Pantosti, D. (2008). Twenty years of paleoseismology in Italy. *Earth-Science Rev.* 88, 89–117. doi:10.1016/j.earscirev.2008.01.001

Giaccio, B., Niespolo, E. M., Pereira, A., Nomade, S., Renne, P. R., Albert, P. G., et al. (2017). First integrated tephrochronological record for the last 190 kyr from the Fucino Quaternary lacustrine succession, central Italy. *Quat. Sci. Rev.* 158, 211–234. doi:10.1016/j.quascirev.2017.01.004

Giaccio, B., Leicher, N., Mannella, G., Monaco, L., Regattieri, E., Wagner, B., et al. (2019). Extending the tephra and palaeoenvironmental record of the Central mediterranean back to 430 ka: a new core from Fucino Basin, Central Italy. *Quat. Sci. Rev.* 225, 106003. doi:10.1016/j.quascirev.2019.106003

Giaccio, B., Wagner, B., Zanchetta, G., Bertini, A., Cavinato, G. P., De Franco, R., et al. (2024). International Continental Scientific Drilling Program (ICDP) workshop on the Fucino paleolake project: the longest continuous terrestrial archive in the MEditerranean recording the last 5 million years of Earth system history (MEME). *Sci. Dril* 33, 249–266. doi:10.5194/sd-33-249-2024

Giraudi, C. (1988). Faglie ad attività olocenica nella Piana del Fucino. *Mem. Della Soc. Geol. Ital.* 35, 875–880.

Gold, R. D., Stephenson, W. J., Briggs, R. W., DuRoss, C. B., Kirby, E., Woolery, E., et al. (2020). Seismic reflection imaging of the low-angle Panamint normal fault system, eastern California. *J. Geophys. Res. Solid Earth* 125 (11), e2020JB020243. doi:10.1029/2020jb020243

Haberland, C., Gibert, L., Jurado, M. J., Stiller, M., Baumann-Wilke, M., Scott, G., et al. (2017). Architecture and tectono-stratigraphic evolution of the intramontane Baza Basin (Bétics, SE-Spain): constraints from seismic imaging. *Tectonophysics* 709, 69–84. doi:10.1016/j.tecto.2017.03.022

Improta, L., and Bruno, P. P. (2007). Combining seismic reflection with multifold wide aperture profiling: an effective strategy for high resolution shallow imaging of active faults. *Geophys. Res. Lett.* 34, L20310. doi:10.1029/2007GL031893

Konno, K., and Ohmachi, T. (1998). Ground motion characteristics estimated from spectral ratio between horizontal and vertical components of microtremor, 1998. *Bull. Seismol. Soc. Am.* 88 (1), 228–241. doi:10.1785/bssa0880010228

Lanari, R., Faccenna, C., Benedetti, L., Sembroni, A., Bellier, O., Menichelli, I., et al. (2021). Formation and persistence of extensional internally drained basins: the case of the Fucino basin (Central Apennines, Italy). *Tectonics* 40, e2020TC006442. doi:10.1029/2020TC006442

Malinverno, A., and Ryan, W. B. F. (1986). Extension in the Tyrrhenian Sea and shortening in the Apennines as a result of arc migration driven by sinking of the lithosphere. *Tectonics* 5, 227–245. doi:10.1029/TC005i002p00227

Mancinelli, P., Scisciani, V., Patruno, S., and Minelli, G. (2021). Gravity modeling reveals a Messinian foredeep depocenter beneath the intermontane Fucino Basin (Central Apennines). *Tectonophysics* 821, 229144. doi:10.1016/j.tecto.2021.229144

Margheriti, L., Nostro, C., Cocina, O., Castellano, M., Moretti, M., Lauciani, V., et al. (2021). Seismic surveillance and earthquake monitoring in Italy. *Seismol. Res. Lett.* 92 (3), 1659–1671. doi:10.1785/0220200380

McNamara, D. E., and Buland, R. P. (2004). Ambient noise levels in the Continental United States. *Bull. Seismol. Soc. Am.* 94 (4), 1517–1527. doi:10.1785/012003001

Michetti, A. M., Brunamonte, F., Serva, L., and Vittori, E. (1996). Trench investigations of the 1915 Fucino earthquake fault scarps (Abruzzo, Central Italy): geological evidence of large historical events. *J. Geophys. Res.* 101, 5921–5936. doi:10.1029/95jb02852

Molnar, S., Sirohey, A., Assaf, J., Bard, P. Y., Castellaro, S., Cornou, C., et al. (2022). A review of the microtremor horizontal-to-vertical spectral ratio (MHVSR) method. *J. Seismol.* 26 (4), 653–685. doi:10.1007/s10950-021-10062-9

Mondati, G., Spadi, M., Gliozzi, E., Cosentino, D., Cifelli, F., Cavinato, G. P., et al. (2021). The tectono-stratigraphic evolution of the Fucino Basin (central Apennines, Italy): new insights from the geological mapping of its north-eastern margin. *J. Maps* 17 (2), 87–100. doi:10.1080/17445647.2021.1880981

Nakamura, Y. (1989). A method for dynamic characteristics estimation of subsurface using microtremor on the ground surface. *QR RTRI* 30, 25–33.

Oddone, G. (1915). Gli elementi fisici del grande terremoto marsicano fucense del 13 gennaio 1915. *Boll. Soc. Sismol. Ital.* 19, 71–215.

Papanikolaou, I. D., Roberts, G. P., and Michetti, A. M. (2005). Fault scarps and deformation rates in Lazio-Abruzzo, Central Italy: Comparison between geological fault slip-rate and GPS data. *Tectonophysics* 408 (1-4), 147–176. doi:10.1016/j.tecto.2005.05.043

Patacca, E., Scandone, P., Di Luzio, E., Cavinato, G. P., and Parotto, M. (2008). Structural architecture of the central Apennines: interpretation of the CROP11 seismic profile from the Adriatic coast to the orographic divide. *Tectonics* 27, 1–36. doi:10.1029/2005TC001917

Patruno, S., and Scisciani, V. (2021). Testing normal fault growth models by seismic stratigraphic architecture: the case of the Pliocene-Quaternary Fucino Basin (Central Apennines, Italy). *Basin Res.* 33, 2118–2156. doi:10.1111/bre.12551

Peterson, J. (1993). Open-File Report 93-222. *Observations and modeling of seismic background noise*. doi:10.3133/ofr93322

Rovida, A., Locati, M., Camassi, R., Lolli, B., Gasperini, P., and Antonucci, A. (2021). Data from: Catalogo Parametrico dei Terremoti Italiani CPTI15, versione 3.0. *Istituto Nazionale di Geofisica e Vulcanologia (INGV)*. doi:10.13127/CPTI/CPTI15.3

Schimmel, M., and Paulssen, H. (1997). Noise reduction and detection of weak, coherent signals through phase-weighted stacks. *Geophys. J. Int.* 130 (2), 497–505. doi:10.1111/j.1365-246x.1997.tb05664.x

Serva, L., Blumetti, A. M., and Michetti, A. M. (1988). Gli effetti sul terreno del terremoto del Fucino (13 gennaio 1915); tentativo di interpretazione dell'evoluzione tettonica recente di alcune strutture. *Mem. Della Soc. Geol. Ital.* 35, 893–907.

Stephenson, W. J., Odum, J. K., Williams, R. A., McBride, J. H., and Tomlison, I. (2012). Characterization of intrabasin faulting and deformation for earthquake hazards in Southern Utah Valley, Utah, from high-resolution seismic imaging. *Bull. Seismol. Soc. Am.* 102 (2), 524–540. doi:10.1785/0120110053

Stephenson, W. J., Frary, R. N., Louie, J., and Odum, J. K. (2013). Quaternary extensional growth folding beneath Reno, Nevada, imaged by urban seismic profiling. *Bull. Seismol. Soc. Am.* 103 (5), 2921–2927. doi:10.1785/0120120311

Strecker, U., Steidtmann, J. R., and Smithson, S. B. (1999). Conceptual tectonostratigraphic model for seismic facies migrations in a fluvio-lacustrine extensional basin. *AAPG Bull.*, V. 83, No. 1 (January 1999), P. 43–61.

Vardy, M. E., L'Heureux, J. S., Vanneste, M., Longva, O., Steiner, A., Forsberg, C. A., et al. (2012). Multidisciplinary investigation of a shallow near-shore landslide, Finneidfjord, Norway. *Near Surf. Geophys.* 10, 267–277. doi:10.3997/1873-2012022

Vassallo, M., De Matteis, R., Bobbio, A., Di Giulio, G., Adinolfi, G. M., Cantore, L., et al. (2019). Seismic noise cross-correlation in the urban area of Benevento city (Southern Italy). *Geophys. J. Int.* 217 (3), 1524–1542. doi:10.1093/gji/ggz101

Vassallo, M., Riccio, G., Mercuri, A., Cultrera, G., and Di Giulio, G. (2022). HV noise and earthquake automatic analysis (HVNEA). *Seismol. Res. Lett.* 94 (1), 350–368. doi:10.1785/0220220115

Villani, F., Maraio, S., Bruno, P. P., Improta, L., Wood, K., Pucci, S., et al. (2021). High-Resolution seismic profiling in the hanging Wall of the Southern fault section ruptured during the 2016 Mw 6.5 central Italy earthquake. *Tectonics* 40 (9), e2021TC006786. doi:10.1029/2021tc006786

Villani, F., Maraio, S., Improta, L., Sapia, V., Di Giulio, G., Baccheschi, P., et al. (2024). High-resolution geophysical investigations in the central Apennines seismic belt (Italy): results from the Campo Felice tectonic basin. *Tectonophysics* 871, 230170. doi:10.1016/j.tecto.2023.230170

Wathelet, M., Guillier, B., Roux, P., Cornou, C., and Ohrnberger, M. (2018). Rayleigh wave three-component beamforming: signed ellipticity assessment from high-resolution frequency-wavenumber processing of ambient vibration arrays. *Geophys. J. Int.* 215 (1), 507–523. doi:10.1093/gji/ggy286

Wathelet, M., Chatelain, J. L., Cornou, C., Di Giulio, G., Guillier, B., Ohrnberger, M., et al. (2020). Geopsy: a user-friendly open-source tool set for ambient vibration processing. *Seismol. Res. Lett.* 91 (3), 1878–1889. doi:10.1785/0220190360